

## CHAPTER 5

# The Parallel Resonant Converter

The objective of this chapter is to describe the operation of the parallel resonant converter in detail. The concepts developed in chapter 3 are used to derive closed-form solutions for the output characteristics and steady-state control characteristics, to determine operating mode boundaries, and to find peak component stresses. General results are presented using frequency control for both the continuous and the discontinuous conduction modes. This chapter also explains the origin of the discontinuous conduction mode, which is in many ways the dual of the series resonant discontinuous conduction mode.

The characteristics of the parallel resonant converter are quite different from those of the series resonant converter, and from those of conventional PWM converters. The parallel topology can both step up and step down the dc voltage. Although the output characteristics are again elliptical, near resonance they exhibit a current-source characteristic. The discontinuous conduction mode occurs under heavy loading (or short-circuit conditions, in the limit). The transistor current stresses and conduction loss depend on the output voltage, and are nearly independent of load current.

Although these features may make the parallel resonant converter ill-suited to some conventional power supply applications, they can be used to advantage in others. An example is given in section 5.4, in which the parallel resonant converter is used to construct a 24V:10kV high voltage power supply with current source characteristics. Design considerations are outlined, and the near-ideal operation of an experimental circuit is described. A second application example is also explored, in which the parallel resonant converter is used as an off-line low harmonic rectifier. The converter input characteristics are found, and the advantages and disadvantages of the PRC in this application are discussed.

### 5.1. Ideal Steady-State Characteristics in the Continuous Conduction Mode

A full bridge isolated version of the parallel resonant converter is given in Fig. 5.1. For this discussion, a 1:1 turns ratio is assumed. The converter differs from the series resonant converter because it is the tank capacitor voltage, rather than the tank inductor current, which is rectified and filtered to produce the dc load voltage. A two-pole L-C low pass filter ( $L_F$  and  $C_F$ ) performs this filter function. Hence, we have

$$V = \langle |v_C| \rangle \quad (5-1)$$

by use of the flux-linkage balance principle (Chapter 3) on inductor  $L_F$ . The magnitude of the quasi-sinusoidal voltage  $v_C(t)$  is controllable by variation of the switching frequency —  $v_C$  becomes large in amplitude near resonance. Hence, the dc output voltage  $V$  is controllable by variation of the normalized switching frequency  $F = f_S / f_0$ .

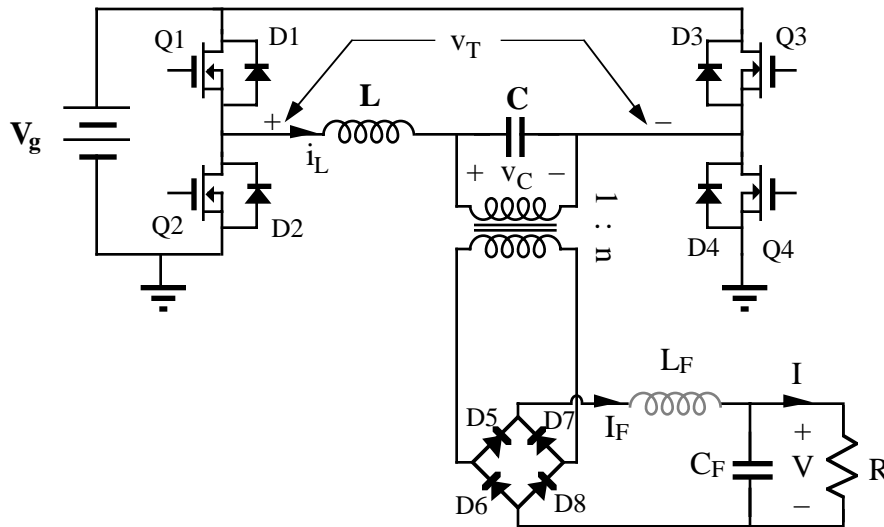


Fig. 5.1. Full bridge realization of the parallel resonant converter.

The  $L_F$  and  $C_F$  filter elements are “large”, i.e., their switching ripple components are small compared to their respective dc components in a well-designed converter. Hence,  $I_F$  and  $V$  are essentially dc. Also, by charge balance on  $C_F$ , we have in steady-state

$$I_F = I \quad (5-2)$$

Typical waveforms are drawn in Fig. 5.2 for above-resonance operation with zero voltage switching. The input bridge produces a square wave output voltage  $v_T(t)$ , which is applied across the LC tank circuit. In response, the tank current and tank capacitor voltage ring with quasi-sinusoidal voltages. The bridge rectifier now switches when the tank voltage passes through zero. The peak values of the tank waveforms  $v_C(t)$  and  $i_L(t)$  do not, in general, occur at the transistor or

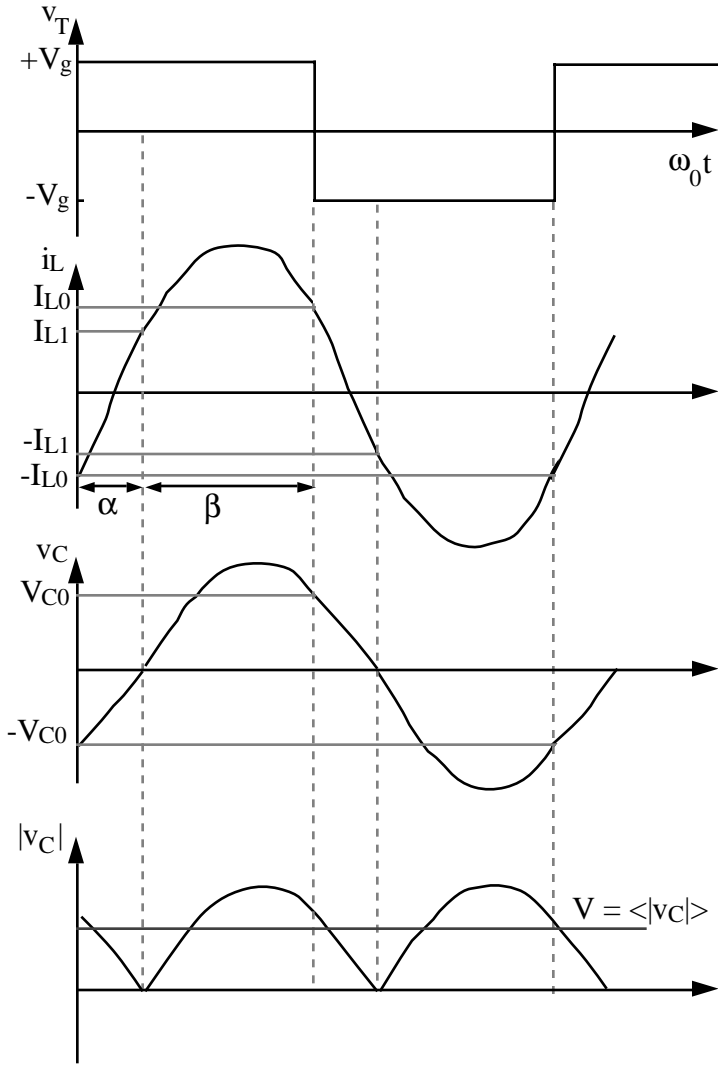


Fig. 5.2. Typical waveforms for the parallel resonant converter operating in continuous conduction mode.

diode switching times. In the continuous conduction mode, four subintervals occur during each switching period. The circuit topologies during these subintervals depend on the conducting states of the input and output bridges, which in turn depend on the input bridge drive signal and the polarity of the tank capacitor voltage.

The tank circuits during each of the four subintervals are drawn in Figs. 5.3 – 5.6. In each case, the tank circuit topology is identical to that of Fig. 3.15, repeated in Fig. 5.7. The applied tank voltage  $V_T$  is  $\pm V_g$ , depending on the conducting states of the input bridge switches, and the applied tank current  $I_T$  is  $\pm I_F (= \pm I)$ , depending on the polarity of the tank capacitor voltage. These voltages are summarized in Table 5.1.

**Table 5.1. Applied tank voltages and currents for the parallel resonant converter operating in continuous conduction mode**

Interval	$V_T$	$M_T$	$I_T$	$J_T$
1	$+V_{\varepsilon g}$	+1	-I	-J
2	$+V_{\varepsilon g}$	+1	+I	+J
3	$-V_{\varepsilon g}$	-1	+I	+J
4	$-V_{\varepsilon g}$	-1	-I	-J

**Subinterval 1**      Q1, Q4, D6, D7 conduct  
 $v_C < 0$   
 $0 < \omega_0 t < \alpha$

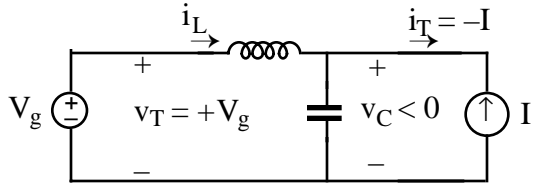


Fig. 5.3. Tank circuit during subinterval 1.

**Subinterval 2**      Q1, Q4, D5, D8 conduct  
 $v_C > 0$   
 $\alpha < \omega_0 t < \alpha + \beta = \gamma$

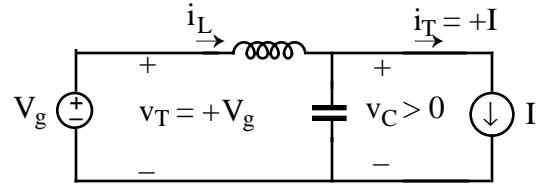


Fig. 5.4. Tank circuit during subinterval 2.

**Subinterval 3**      Q2, Q3, D5, D8 conduct  
 $v_C > 0$   
 $\gamma < \omega_0 t < \gamma + \alpha$

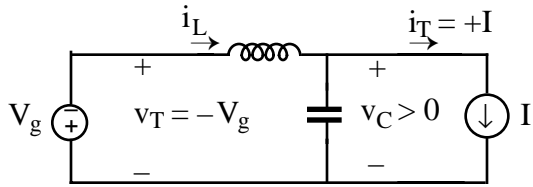


Fig. 5.5. Tank circuit during subinterval 3.

**Subinterval 4**      Q2, Q3, D6, D7 conduct  
 $v_C < 0$   
 $\gamma + \alpha < \omega_0 t < 2\gamma$

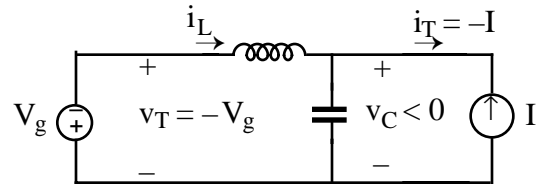


Fig. 5.6. Tank circuit during subinterval 4.

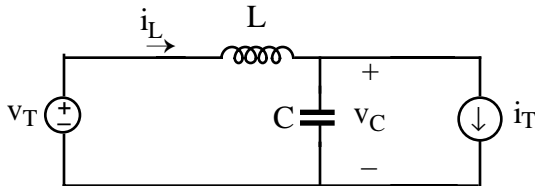


Fig. 5.7. General form of tank circuit topology.

### State plane portrait

The normalized state plane trajectory for the circuit of Figs. 5.7 and 3.15 is derived in section 3.3. As before, the tank waveforms are normalized according to the definitions  $m_C(t) = v_C(t) / V_g$  and  $j_L(t) = i_L(t) R_0 / V_g$ . The result is plotted in Fig. 3.16 and reproduced in Fig. 5.8. The tank circuit solutions follow circular arcs, centered at the applied tank voltage and current values  $(m_C, j_L) = (M_T, J_T)$ , and with radius dependent on the initial values of  $m_C$  and  $j_L$ .

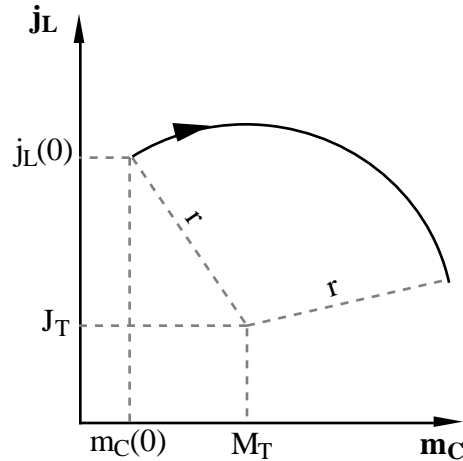
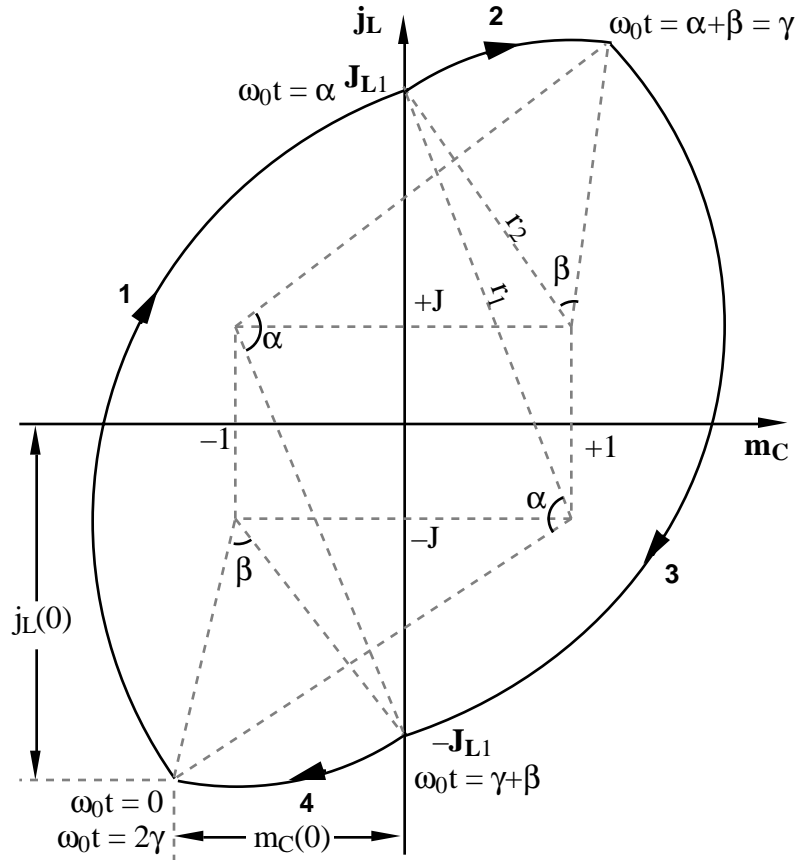


Fig. 5.8. State plane trajectory, for the circuit of Fig. 5.7.

One can now construct the state plane trajectory for a complete switching period in the continuous conduction mode. As shown in Fig. 5.9, the trajectory begins at  $\omega_0 t = 0$ , at the initial point  $(m_C(0), j_L(0)) = (-M_{C0}, -J_{L0})$  for subinterval 1. The tank capacitor voltage must be negative (so that output diodes D6 and D7 conduct and the circuit of Fig. 5.3 applies), and the tank inductor

current is also drawn initially negative for this example. From Table 5.1 and Fig. 5.8, the normalized state plane trajectory follows a circular arc centered at  $(m_C, j_L) = (+1, -J)$ . The radius of this arc  $r_1$  is the distance between the initial point and the center, and remains constant. As the tank rings during the first subinterval, the trajectory moves in the clockwise direction around the center. The first subinterval ends at  $\omega_0 t = \alpha$ , when the tank voltage passes through zero (i.e., when  $m_C$  reaches zero). The normalized tank current at this point is denoted  $J_{L1}$ .



When the tank capacitor voltage passes through zero, output diodes  $D_6$  and  $D_7$  turn

off, and diodes  $D_5$  and  $D_8$  turn on. The circuit of Fig. 5.4 is then obtained, and the normalized state plane trajectory then follows a circular arc centered at  $(m_C, j_L) = (+1, +J)$ . The radius  $r_2$  of this arc is the distance between the initial point  $(0, J_{L1})$  and the center  $(+1, +J)$ . The trajectory moves in the clockwise direction around the center. This subinterval ends at  $\omega_0 t = (\alpha + \beta) = \gamma$ , when the transistors  $Q_1$  and  $Q_4$  are turned off and  $Q_2$  and  $Q_3$  are turned on.

When the converter operates in steady-state with symmetrical transistor drive waveforms, the state-plane trajectory is symmetrical. During the third subinterval, the trajectory is a circular arc centered at  $(-1, +J)$  which ends when the tank capacitor voltage passes through zero and the output diodes switch. The trajectory then continues in the fourth subinterval with the center  $(-1, -J)$ . This subinterval ends when transistors  $Q_2$  and  $Q_3$  are turned off, ending the switching period at  $\omega_0 t = 2\gamma$ . If the converter operates in steady-state, then the ending point  $(m_C(2\gamma), j_L(2\gamma))$  coincides with the initial point  $(m_C(0), j_L(0))$ , and the state plane trajectory is closed.

**Averaging and flux linkage arguments**

It is desired to solve for the converter steady-state output characteristics implied by the closed state-plane trajectory of Fig. 5.9. This task can involve quite a bit of algebraic manipulations, but is considerably simplified when the averaging and flux-linkage arguments of chapter 3 are used first. A simple relation between the converter dc output voltage and the normalized tank current boundary value  $J_{L1}$  is found here, which then is used in the next section to determine the converter output characteristics.

A simplified schematic of the parallel resonant converter is given in Fig. 5.10, in which the input voltage  $V_g$  and bridge transistors and diodes are replaced by an equivalent square-wave voltage source  $v_T(t)$ . The voltage waveform  $v_T(t)$ , as well as the tank capacitor and inductor voltage waveforms  $v_C(t)$  and  $v_L(t)$  are plotted in Fig. 5.11 for a typical steady-state operating point.

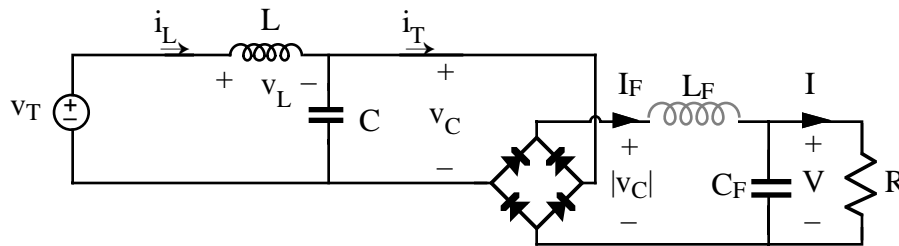


Fig. 5.10. Simplified diagram of the parallel resonant converter, illustrating use of averaging and flux linkage arguments.

As described in Eq. (5-1), in steady-state there is no dc component of voltage across the output filter inductor  $L_F$ , and hence the dc output voltage  $V$  is equal to the average value of the rectified tank capacitor voltage  $\langle |v_C| \rangle$ . As seen in Fig. 5.11, the tank capacitor voltage is positive over the second and third subintervals, and is negative but symmetric during the fourth and first subintervals. Hence, the average over the second and third subintervals of the tank capacitor voltage must also equal the output voltage, and Eq. (5-1) becomes

$$V = \frac{2}{T_s} \int_{t_a}^{t_a + \frac{1}{2}T_s} v_C(t) dt \tag{5-3}$$

where  $t_a = \alpha/\omega_0$  is the time at the beginning of the second subinterval. Equation (5-3) can be rewritten

$$V = \frac{2}{T_s} \lambda_C \tag{5-4}$$

where

$$\lambda_C = \int_{t_a}^{t_a + \frac{1}{2}T_s} v_C(t) dt \tag{5-5}$$

is the tank capacitor volt-seconds over the second and third subintervals, as illustrated in Fig. 5.11.

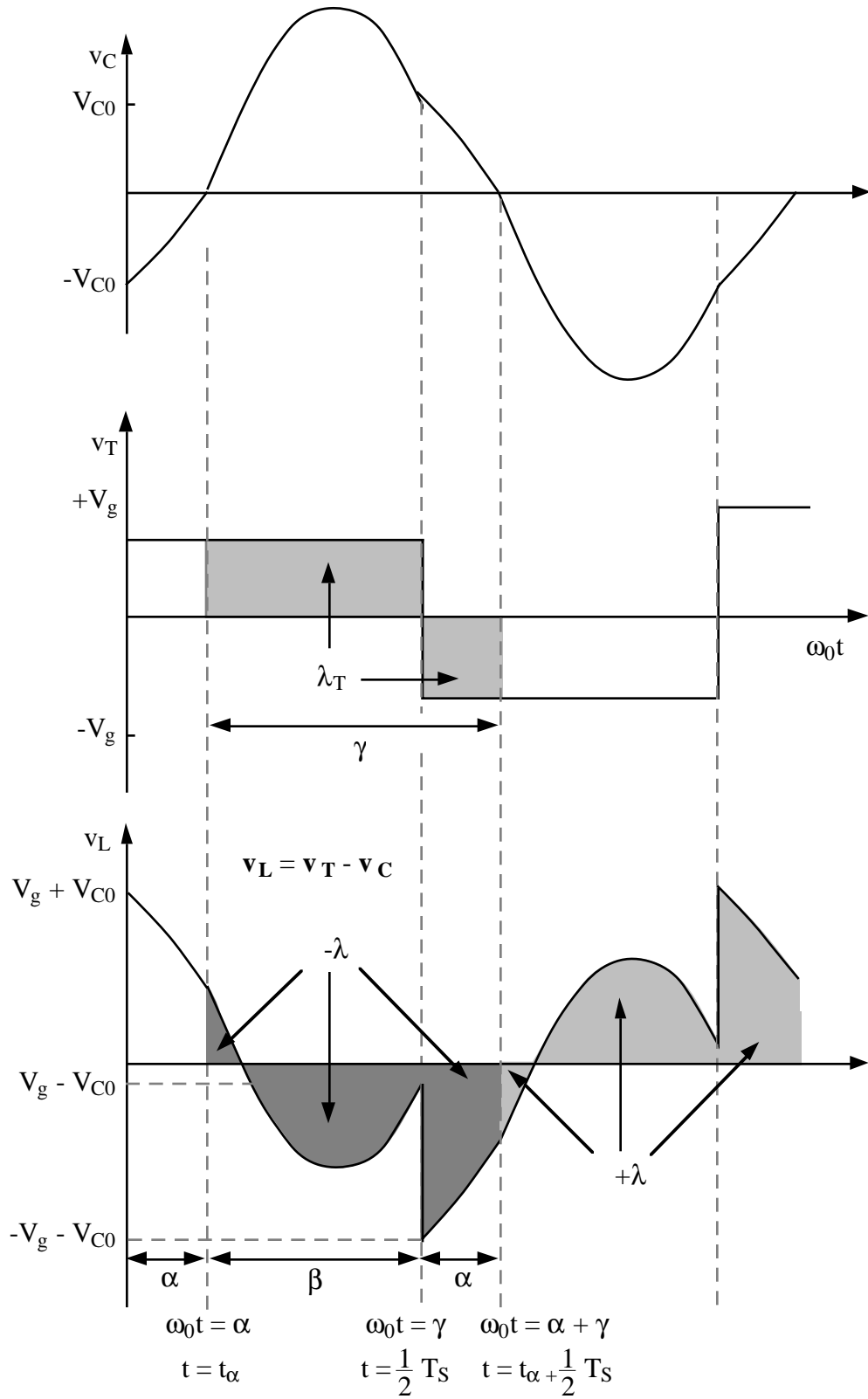


Fig. 5.11. Tank waveforms and flux linkages, over one switching period.

We can now use Kirchoff's Laws in integral form, as described in Chapter 3, to solve the tank circuit of Fig. 5.10, and hence relate  $\lambda_C$  to the tank inductor current waveform. In particular, by Kirchoff's voltage law, we have  $v_C(t) = v_T(t) - v_L(t)$ . Upon integration over the second and third subintervals, this becomes

$$\lambda_C = \lambda_T - \lambda_L \quad (5-6)$$

where

$$\lambda_T = \int_{t_a}^{t_a + \frac{1}{2}T_S} v_T(t) dt \quad (5-7)$$

$$\lambda_L = \int_{t_a}^{t_a + \frac{1}{2}T_S} v_L(t) dt \quad (5-8)$$

Substitution of Eq. (5-6) into Eq. (5-4) yields

$$V = \frac{2}{T_S} (\lambda_T - \lambda_L) \quad (5-9)$$

The quantities  $\lambda_T$  and  $\lambda_L$  can now be found using some simple arguments.

The applied voltage  $v_T(t)$  is a square wave, and hence evaluation of the integral in Eq. (5-7) leads to

$$\lambda_T = V_g \left( \frac{1}{2}T_S - 2t_a \right) = V_g \frac{(\beta - \alpha)}{\omega_0} \quad (5-10)$$

The quantity  $\lambda_L$  is the volt-seconds applied to the tank inductor over the second and third subintervals, and can be related to the tank current using the tank inductor flux linkage variation arguments of Chapter 3. From Fig. 5.2, over these two intervals the tank inductor current changes from the value  $+I_{L1}$  to  $-I_{L1}$ , for a total change of  $-2I_{L1}$ . This change is related to the applied volt-seconds or flux linkages  $\lambda_L$  (see Eq. 3-7) by

$$\lambda_L = L (-2I_{L1}) \quad (5-11)$$

Substitution of Eqs. (5-10) and (5-11) into Eq. (5-9) gives

$$V = \frac{2}{T_S} \left( V_g \frac{\beta - \alpha}{\omega_0} + 2LI_{L1} \right) \quad (5-12)$$

Normalization of this expression yields

$$\frac{M\gamma}{2} = (\varphi + J_{L1}) \quad (5-13)$$

where

$$\varphi = \frac{\beta - \alpha}{2} \quad (5-14)$$

This is the desired result. Equation (5-13) is used in the next section to relate the converter voltage conversion ratio  $M$  to the state plane diagram via the inductor current boundary value  $J_{L1}$ .

### *Solution of state plane diagram*

The somewhat lengthy details of the solution of the state plane diagram for the closed trajectory in steady state are outlined here for the interested student. The results of this analysis are closed-form expressions for  $J_{L1}$  and  $\varphi$  in terms of the normalized load current  $J$  and angular switching half-period  $\gamma$ , which can be substituted into Eq. (5-13) to determine the converter steady-state output characteristics. Other quantities of interest are also found, which allow determination of peak component stresses and zero-current- / zero-voltage-switching boundaries.

In steady state, the state plane trajectory of Fig. 5.9 is closed, and the ending point for  $\omega_0 t = 2\gamma$  coincides with the initial point at  $\omega_0 t = 0$ . For a given converter operating point, there is a unique set of values of angles  $\alpha$  and  $\beta$ , radii  $r_1$  and  $r_2$ , and boundary values  $J_{L1}$ ,  $J_{L0}$ , and  $M_{C0}$ . These quantities are found by equating the initial and final points. Because of the symmetry of the state plane trajectory, an equivalent steady-state condition is that the second subinterval (which begins at  $\omega_0 t = \alpha$  at the point  $(0, J_{L1})$ ) should end at  $\omega_0 t = \gamma$  at point  $(M_{C0}, J_{L0})$ , coinciding with the beginning point of the third subinterval (which ends at the point  $(0, -J_{L1})$ ). This steady-state boundary condition is matched below. First, the arc radii  $r_1$  and  $r_2$  are found. The tank capacitor voltage boundary condition  $M_{C0}$  and the tank inductor current boundary condition  $J_{L0}$  are then matched. The quantities  $J_{L1}$  and  $j$  are then found, and are substituted into Eq. (5-13) to give the closed-form converter output characteristic.

Determine arc radii  $r_1, r_2$

An expanded view of the upper left portion of the state plane diagram is given in Fig. 5.12. From the solution of triangle  $ABC$ , we have

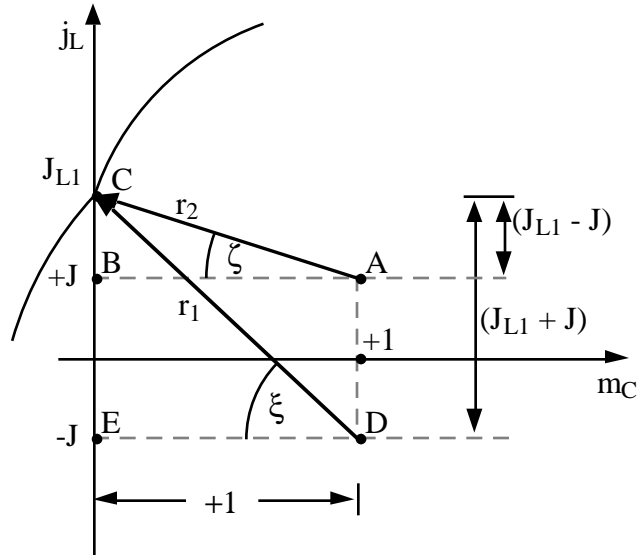
$$r_2 \sin \zeta = (J_{L1} - J) \quad (5-15)$$

$$r_2 \cos \zeta = 1 \quad (5-16)$$

Likewise, from the solution of triangle  $DEC$ , we have

$$r_1 \sin \xi = (J_{L1} + J) \quad (5-17)$$

$$r_1 \cos \xi = 1 \quad (5-18)$$



(5-18) Fig. 5.12. Magnified view of state plane trajectory, illustrating arc radii.

Match boundary condition on  $J_{L0}$

The right half of the state plane trajectory is redrawn in Fig. 5.13 for the above resonance case. At  $\omega_0 t = \gamma$  (after one half switching period), the normalized tank inductor current is  $j_L(\gamma) = J_{L0}$ .

Subinterval 2 begins at  $j_L(\alpha) = J_{L1}$ . The trajectory travels around the arc of radius  $r_2$  centered at  $(+1, +J)$ . The final value of  $j_L$  for this subinterval is  $J + r_2 \sin(\pi - \beta - \zeta)$ , as shown in Fig. 5.13. By equating this value to  $J_{L0}$ , we have

$$\begin{aligned} J_{L0} &= J + r_2 \sin(\pi - \beta - \zeta) \\ &= J + r_2 \sin(\beta + \zeta) \end{aligned} \quad (5-19)$$

In steady state, subinterval 3 ends at the point  $j_L(\gamma + \alpha) = -J_{L1}$ . The trajectory is an arc centered at  $(-1, +J)$  with radius  $r_1$ . Under these conditions, the initial value of tank inductor current is  $j_L(\gamma) = J + r_1 \sin(\alpha - \xi)$ , by solution

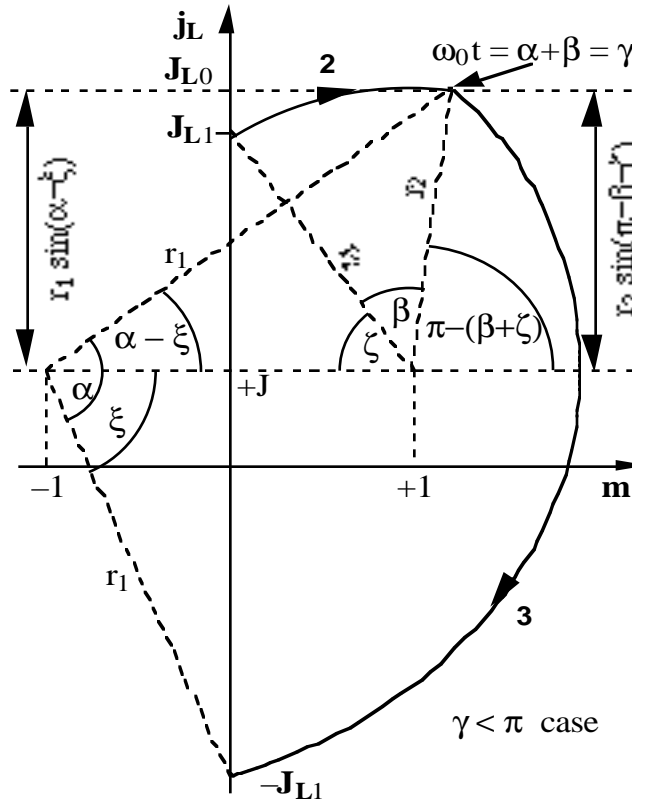


Fig. 5.13. Magnified view of right half portion of state plane trajectory, illustrating boundary conditions on  $J_{L0}$ .

of Fig 5.13. By equating this value to  $J_{L0}$ , we have

$$J_{L0} = J + r_1 \sin (\alpha - \xi) \quad (5-20)$$

One can now equate Eqs. (5-19) and (5-20) to obtain

$$r_2 \sin (\beta + \zeta) = r_1 \sin (\alpha - \xi) \quad (5-21)$$

Use of a trigonometric identity for the sine of the sum of angles yields

$$r_2 (\sin \beta \cos \zeta + \cos \beta \sin \zeta) = r_1 (\sin \alpha \cos \xi - \cos \alpha \sin \xi) \quad (5-22)$$

The quantities  $r_2 \cos \zeta$ ,  $r_2 \sin \zeta$ ,  $r_1 \cos \xi$ , and  $r_1 \sin \xi$  may now be eliminated using Eqs. (5-15) - (5-18). The result is

$$\sin \alpha - (J_{L1} + J) \cos \alpha = \sin \beta + (J_{L1} - J) \cos \beta \quad (5-23)$$

By now collecting terms, using trigonometric identities, and noting that  $(\alpha+\beta)/2 = \gamma/2$  and  $(\beta-\alpha)/2 = \varphi$ , one obtains the result

$$-\sin \varphi \left( \cos \frac{\gamma}{2} + J \sin \frac{\gamma}{2} \right) = J_{L1} \cos \frac{\gamma}{2} \cos \varphi \quad (5-24)$$

*Match boundary conditions on  $M_{C0}$*

The capacitor voltage boundary conditions are matched in a similar way. Refer to Fig. 5.14. At  $\omega_0 t = \gamma$  (after one half switching period), the normalized tank capacitor voltage is  $m_C(\gamma) = M_{C0}$ .

Subinterval 2 begins at  $m_C(\alpha) = 0$ . The trajectory travels around the arc of radius  $r_2$  centered at  $(+1, +J)$ . It can be seen from Fig. 5.14 that the final value of  $m_C$  for this subinterval is  $1 + r_2 \cos(\pi - \beta - \zeta)$ . By equating this value to  $M_{C0}$ , we have

$$\begin{aligned} M_{C0} &= 1 + r_2 \cos(\pi - \beta - \zeta) \\ &= 1 - r_2 \cos(\beta + \zeta) \end{aligned} \quad (5-25)$$

In steady state, subinterval 3 ends at the point  $m_C(\gamma + \alpha) = 0$ . The trajectory is an arc centered at  $(-1, +J)$  with radius  $r_1$ . Under these conditions, the initial value of tank capacitor voltage is  $m_C(\gamma) = r_1 \cos(\alpha - \xi) - 1$ , by solution of Fig 5.14. Equating this value to  $M_{C0}$  yields

$$M_{C0} = r_1 \cos(\alpha - \xi) - 1 \quad (5-26)$$

One can now equate Eqs. (5-25) and (5-26) to obtain

$$1 - r_2 \cos(\beta + \zeta) = r_1 \cos(\alpha - \xi) - 1 \quad (5-27)$$

The solution for  $M_{C0}$  follows the same steps and uses the same trigonometric identities as the solution for  $J_{L0}$ , and it yields the following result:

$$\cos \varphi \left( \cos \frac{\gamma}{2} + J \sin \frac{\gamma}{2} \right) = J_{L1} \cos \frac{\gamma}{2} \sin \varphi + 1 \quad (5-28)$$

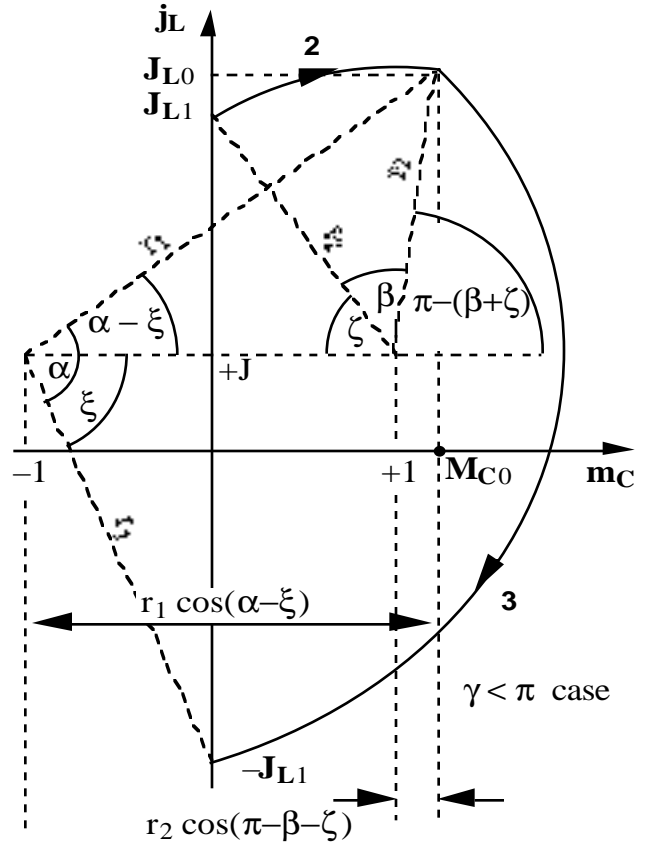


Fig. 5.14. Magnified view of right half portion of state plane trajectory, illustrating boundary conditions on  $M_{C0}$ .

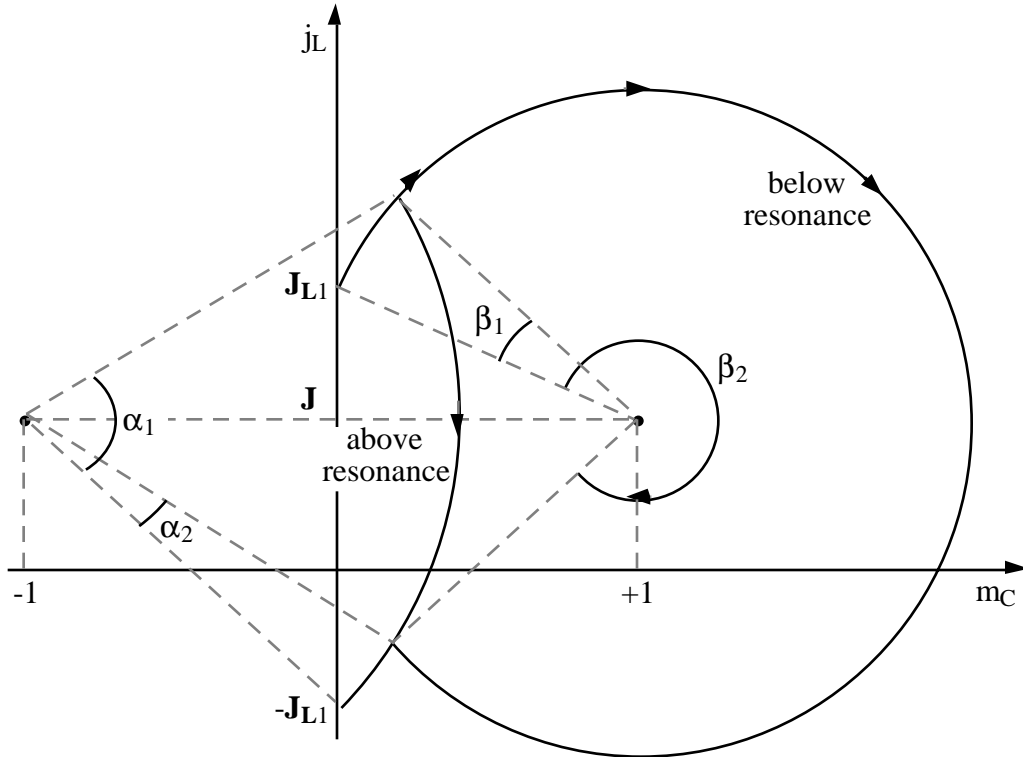


Fig. 5.15. Two possible trajectories for a given value of  $M$  and  $J$ , corresponding to angle  $\varphi$  of equal magnitude and opposite polarity.

*Find solution*

An expression for  $\varphi$  is now found by eliminating the term  $J_{L1} \cos(\gamma/2)$  from Eqs. (5-24) and (5-28). By multiplying Eq. (5-24) by  $\sin \varphi$ , multiplying Eq. (5-28) by  $\cos \varphi$ , and subtracting, one obtains

$$\cos \varphi = \cos \frac{\gamma}{2} + J \sin \frac{\gamma}{2} \quad (5-29)$$

One can now solve for  $\varphi$  in terms of  $\gamma$  and  $J$ , to obtain

$$\varphi = \pm \cos^{-1} \left( \cos \frac{\gamma}{2} + J \sin \frac{\gamma}{2} \right) \quad (5-30)$$

with  $0 \leq \cos^{-1}(\bullet) \leq \pi$ .

Which sign should be chosen in Eq. (5-30) for the arc cosine function? For a given equilibrium choice of  $M$  and  $J$ , there are two possible values of  $\gamma$ ; i.e., the same output is obtained at one value of  $\gamma$  above resonance and at another value of  $\gamma$  below resonance. This behavior has previously been observed for the parallel resonant converter in Chapter 2. Figure 5.15 illustrates state plane trajectories for two such solutions, in which  $\varphi$  is equal in magnitude but opposite in polarity. The two trajectories have the same values of  $J$  and  $J_{L1}$ . For the above resonance

trajectory,  $\varphi_1 = (\beta_1 - \alpha_1)/2$  is negative, while  $\varphi_2 = (\beta_2 - \alpha_2)/2$  is positive for the below resonance trajectory. It can be shown that  $\varphi$  is zero at resonance, and hence we obtain

$$\varphi = \begin{cases} -\cos^{-1}\left(\cos\frac{\gamma}{2} + J\sin\frac{\gamma}{2}\right), & \text{for } 0 < \gamma < \pi \text{ (above resonance)} \\ +\cos^{-1}\left(\cos\frac{\gamma}{2} + J\sin\frac{\gamma}{2}\right), & \text{for } \pi < \gamma < 2\pi \text{ (below resonance)} \end{cases} \quad (5-31)$$

This is the desired closed-form solution for  $\varphi$ , in terms of  $\gamma$  and  $J$ .

This expression for  $\varphi$  can now be substituted into the previous boundary condition equations to find similar solutions for the other quantities of interest. The results are

$$J_{L1} = -\frac{\sin\varphi}{\cos\frac{\gamma}{2}} \quad (5-32)$$

$$J_{L0} = -(J^2 - 1)\tan\frac{\gamma}{2} \quad (5-33)$$

$$M_{C0} = -\frac{J\sin\varphi}{\cos\frac{\gamma}{2}} \quad (5-34)$$

These are the desired closed-form solutions for  $J_{L1}$ ,  $J_{L0}$ , and  $M_{C0}$ . They are valid in continuous conduction mode, both above and below resonance.

Finally, one can now substitute Eq. (5-32) into Eq. (5-13) to obtain

$$M = \left(\frac{2}{\gamma}\right)\left(\varphi - \frac{\sin\varphi}{\cos\frac{\gamma}{2}}\right) \quad (5-35)$$

This is the desired closed-form solution for the converter steady-state output characteristics. Given the normalized load current  $J$  and the half-switching-period-angle  $\gamma$ , one can evaluate Eq. (5-31) to find  $\varphi$ , and then evaluate Eq. (5-35) to find the converter voltage conversion ratio  $M$ . In other words, the output voltage can be found for a given load current and switching frequency, without need for computer iteration.

**Output characteristics**

The steady-state output characteristics of the parallel resonant converter operating above and below resonance in the continuous conduction mode, are plotted in Fig. 5.16. This plot was generated using Eqs. (5-31) and (5-35). For given values of normalized switching frequency  $F = f_s / f_0 = \pi / g$ , the relation between the normalized output current  $J$  and the normalized output voltage  $M$  is approximately elliptical. At resonance ( $F=1$ ), the ellipse degenerates to the horizontal line  $J=1$ , and the converter exhibits current source characteristics<sup>1</sup>. Above resonance, the

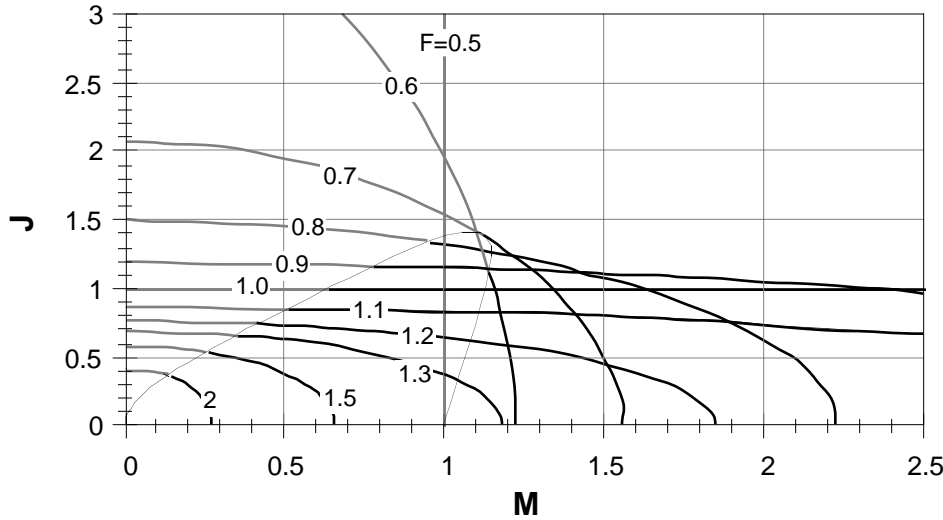


Fig. 5.16. Output characteristics of the parallel resonant converter in the continuous conduction mode. The solid portions of the lines are valid CCM characteristics; shaded portions are invalid.

converter can both step up the voltage ( $M>1$ ) and step down the voltage ( $M<1$ ). The normalized load current is restricted to  $J<1$ , corresponding to  $I<V_g/R_0$ . For a given switching frequency greater than the resonant frequency, the actual limit on maximum

load current is even more restrictive than this limit. Below resonance, the converter can also step up and step down the voltage. Normalized load currents  $J$  greater than one are also obtainable, depending on  $M$  and  $F$ . However, no solutions occur when  $M$  and  $J$  are simultaneously large.

For sufficiently large  $J$ , both above and below resonance, a discontinuous conduction mode can occur (the DCM) which causes the characteristics to deviate from the preceding equations. This mode is discussed in Section 5.2. In consequence, the dashed portions of the lines in Fig. 5.16 are invalid.

The characteristics of Fig. 5.16 look remarkably like ellipses. In fact, these characteristics can be well-approximated by ellipses of the form

$$\frac{M^2}{a^2} + \frac{J^2}{b^2} = 1 \tag{5-36}$$

<sup>1</sup>Actually the converter functions as a gyrator (Fig. 4.36), with gyration conductance  $g = 1/R_0$ .

These approximating ellipses are centered at the origin. The parameters  $a$  and  $b$  can be found by evaluating the open-circuit voltage and closed-circuit current predicted by Eqs. (5-31) and (5-35). The result is

$$a^2 = M^2|_{J=0} = \left(1 - \left(\frac{2}{\gamma}\right) \tan\left(\frac{\gamma}{2}\right)\right)^2 \quad (5-37)$$

$$b^2 = J^2|_{M=0} = \left(\frac{1 - \cos\left(\frac{\gamma}{2}\right)}{\sin\left(\frac{\gamma}{2}\right)}\right)^2 \quad (5-38)$$

Note that  $b$  is not the actual converter short-circuit current because of the existence of the discontinuous conduction mode described later. However, to the extent that the output filter inductor  $L_F$  contains negligible current ripple, it is true that the value  $a$  is the open-circuit voltage. Approximation (5-36) is surprisingly accurate.

### ***Control plane characteristics***

One can now also plot the control plane characteristics, i.e. the output vs. switching frequency for a linear resistive load  $R$ . Define the converter  $Q$  factor as

$$Q = \frac{R}{R_0} \quad (5-39)$$

The normalized load current  $J$  is then related to  $M$  by

$$J = \frac{M}{Q} \quad (5-40)$$

This equation is now used to eliminate  $J$  from the output characteristics. The exact control plane characteristics can be plotted by computer iteration of Eqs. (5-31), (5-35), and (5-40) if desired. Alternatively, the approximate elliptical characteristic of Eq. (5-36) can be used in conjunction with Eq. (5-40) to plot the control plane characteristics in closed form. Substitution of Eq. (5-40) into Eq. (5-36) and solution for  $M$  yields

$$M = \frac{1}{\sqrt{\frac{1}{a^2} + \frac{1}{Q^2 b^2}}} \quad (5-41)$$

where  $a$  and  $b$  are functions of switching frequency and are given by Eqs. (5-37) and (5-38).

The exact control plane characteristics are plotted in Fig. 5.17 for various values of  $Q$ . The exact solution at resonance ( $F=1$ ) is  $M=Q$ . Loading the converter, corresponding to reducing the values of  $Q$  and  $R$ , causes the output voltage to decrease, and results in a less peaked characteristic near resonance. Equation (5-41) gives a good approximation for these curves, except at low  $Q$

(high current) and at low  $F$  (approaching 0.5) because of the existence of the discontinuous conduction mode. This figure was plotted by computer iteration of Eqs. (5-35) and (5-45).

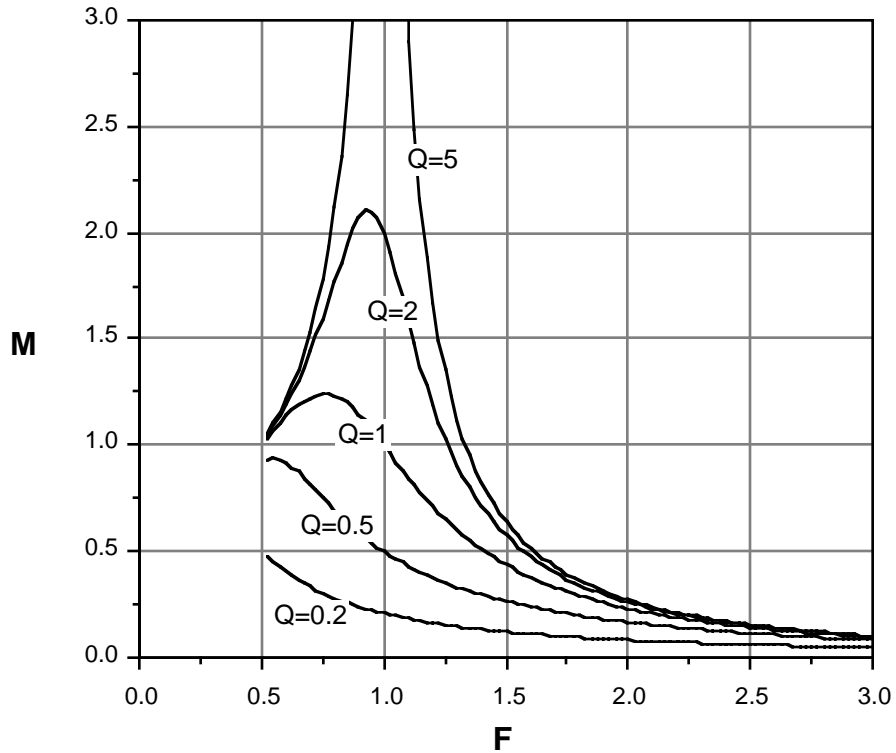


Fig. 5.17. Exact control characteristics of the parallel resonant converter, for  $F > 0.5$ .

## 5.2. Discontinuous Conduction Mode (DCM)

A discontinuous conduction mode mechanism occurs in the parallel resonant converter which is the dual of the discontinuous conduction mode mechanism of the series resonant converter. In this mode, a discontinuous subinterval occurs in which all four output bridge rectifier diodes are forward-biased, and the tank capacitor voltage remains at zero. This mode occurs both above and below resonance when the converter is heavily loaded. In this section, the operation of the converter in the DCM is explained, mode boundaries are found, and the converter output plane characteristics are modified to account for this mode.

### *Reason for occurrence of DCM*

The parallel resonant converter circuit is re drawn in Fig. 5.18(a), with the input switches replaced by an equivalent square-wave voltage source. Typical tank inductor current  $i_L(t)$ , tank capacitor voltage  $v_C(t)$ , tank capacitor current  $i_C(t)$ , and bridge rectifier current  $i_T(t)$  waveforms for

the continuous conduction mode are sketched in Fig. 5.18(b). During the first subinterval  $0 \leq \omega_0 t \leq a$ , the tank capacitor voltage is negative, and hence diodes  $D_6$  and  $D_7$  conduct. Near the end of this subinterval, the tank capacitor current is positive and is equal to  $i_C = i_L + I$ . This causes the tank capacitor voltage to increase towards zero.

Let us consider what happens at time  $\omega_0 t = a$ . The tank capacitor voltage reaches zero, and hence the bridge rectifier diodes attempt to switch such that  $D_6$  and  $D_7$  are reverse-biased, and  $D_5$  and  $D_8$  conduct. The tank capacitor current would then become  $i_C = i_L - I$ . Provided that this new value of  $i_C$  is still positive, the capacitor voltage then continues to increase. This is indeed what happens in the continuous conduction mode, as represented by the waveforms of Fig. 5.18(b).

However, if  $i_C(a^+) = i_L - I$  is negative (i.e., if  $i_L(a) < I$ ) then the capacitor voltage should decrease after the diodes switch. The capacitor voltage would therefore again become negative. But this cannot happen, because the diodes do not switch unless  $v_C$  becomes positive. Hence, diodes  $D_6$  and  $D_7$  cannot turn off at  $\omega_0 t = a$ , and a new discontinuous subinterval occurs in which all four diodes  $D_5$ – $D_8$  conduct.

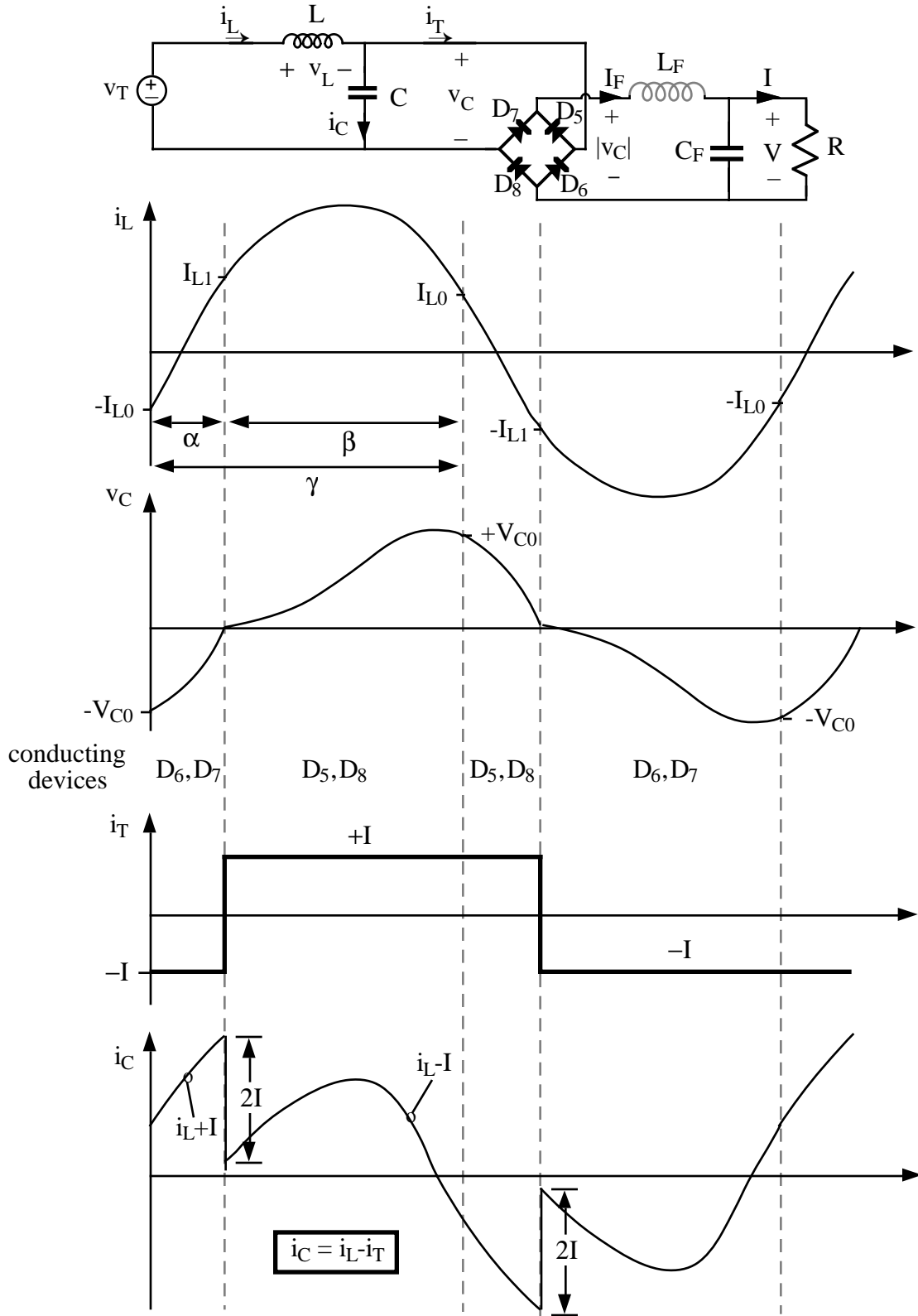
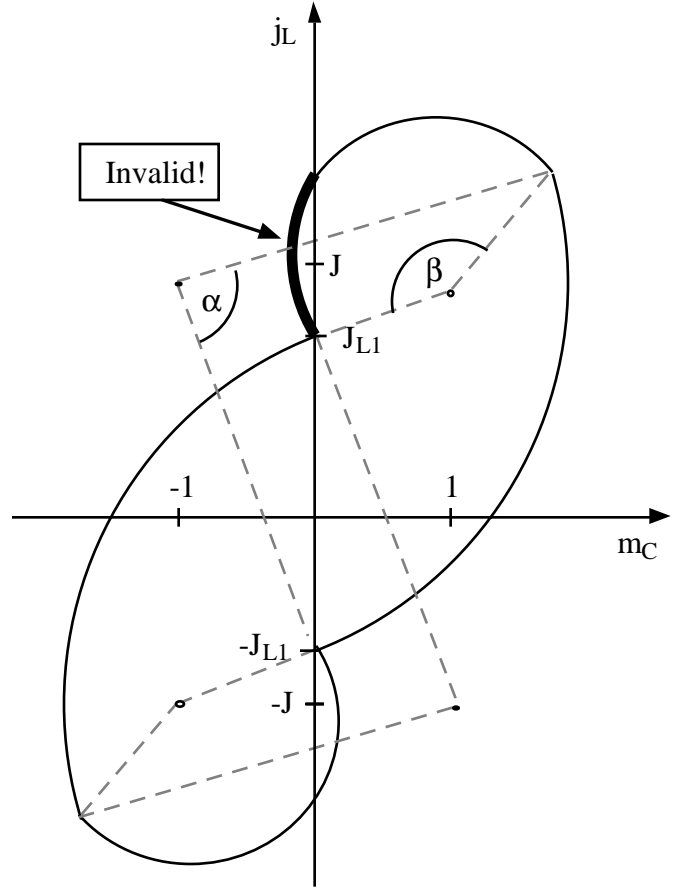


Fig. 5.18. Parallel resonant converter continuous conduction mode operation, near the discontinuous conduction mode boundary: (a) simplified circuit, (b) tank waveforms.

A state-plane interpretation of the reason for the DCM is given in Fig. 5.19. An invalid CCM trajectory is drawn, for which  $J_{L1} < J$ . The trajectory for the second subinterval, corresponding to conduction of diodes  $D_5$  and  $D_8$ , is a circular arc centered at  $m_C = 1, j_L = J$ . This can occur only for  $m_C > 0$ , yet the geometry of the state plane shows that the circular arc must extend into negative values of  $m_C$ . Hence the CCM cannot occur for the operating point illustrated in Fig. 5.19.



*CCM-DCM boundary*

As discussed above, the condition for operation in the DCM is

$$i_L(a) - I < 0 \quad (5-42)$$

In normalized terms,  $j_L(a)$  is  $J_{L1}$ . The closed-form expression for  $J_{L1}$  is given in Eq. (5-32). Hence, Eq. (5-42) can be written

$$J_{L1} < J \quad (5-43)$$

for operation in DCM. Substitution of Eq. (5-32) into Eq. (5-43) and solution for  $J$  yields

$$J > J_{crit} \quad \text{for DCM}$$

$$J < J_{crit} \quad \text{for CCM} \quad (5-44)$$

where 
$$J_{crit} = -\frac{1}{2} \sin(\gamma) + \sqrt{\sin^2\left(\frac{\gamma}{2}\right) + \frac{1}{4} \sin^2(\gamma)}$$

Fig. 5.19. An invalid state plane trajectory, predicted by the CCM analysis.

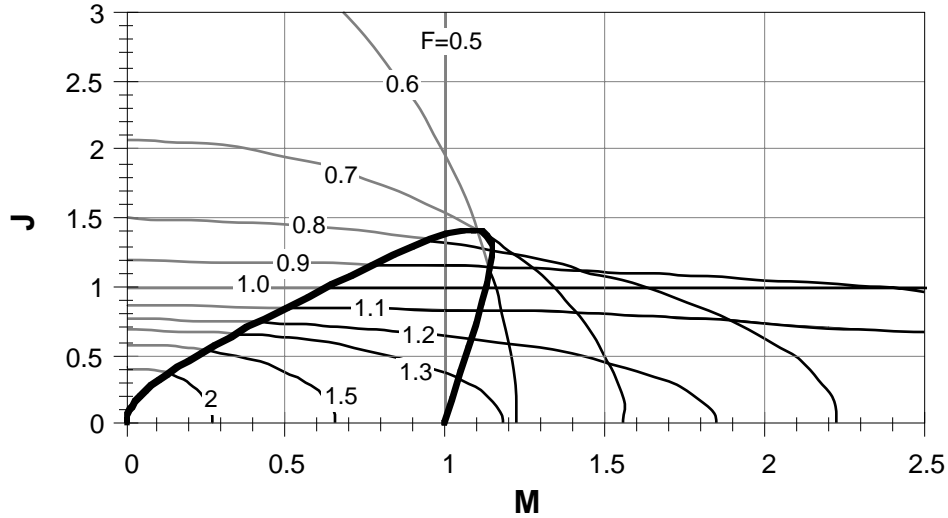


Fig. 5.20. Boundary between the continuous and discontinuous conduction modes (bold line), superimposed on the CCM elliptical characteristics.

The boundary  $J = J_{\text{crit}}$  is plotted as a dotted line in Fig. 5.20. For a given switching frequency,  $J_{\text{crit}}$  is evaluated from Eq. (5-44). The corresponding value of  $M$  on the boundary is then evaluated using Eqs. (5-31) and (5-35). DCM occurs for values of  $J$  above the boundary and  $M$  to the left of the boundary.  $J_{\text{crit}}$  is equal to zero at  $F = 0.5$ , with  $M=1$ ; hence the converter always operates in DCM for  $F = 0.5$ . At resonance,  $J$  is unity, and one can show that the converter operates in DCM for  $M < 2/\pi$ . For frequencies approaching infinity ( $\gamma \rightarrow 0$ ),  $J_{\text{crit}}$  and  $M$  approach zero and the converter always operates in CCM. The double-valued nature of the PRC output characteristics makes Fig. 5.20 somewhat confusing because the output characteristics apparently cross the  $J_{\text{crit}}$  vs.  $M$  curve twice; however, for a given frequency only one of these crossings corresponds to  $J = J_{\text{crit}}$ .

#### DCM solution

The waveforms for the DCM are given in Fig. 5.21. During the discontinuous subinterval ( $a \leq \omega_0 t \leq d$ ), the tank capacitor voltage remains at zero, and all four bridge rectifier diodes  $D_5 - D_8$  conduct. The inductor current increases with constant slope  $V_g/L$ , until, at  $\omega_0 t = d$ ,  $i_L(d) = I$ . At this time, diodes  $D_6$  and  $D_7$  become reverse-biased, and the third subinterval begins. The state plane diagram for the DCM is given in Fig. 5.22.

By state-plane analysis, the steady-state solution for this mode can be determined. The result is the following set of equations:

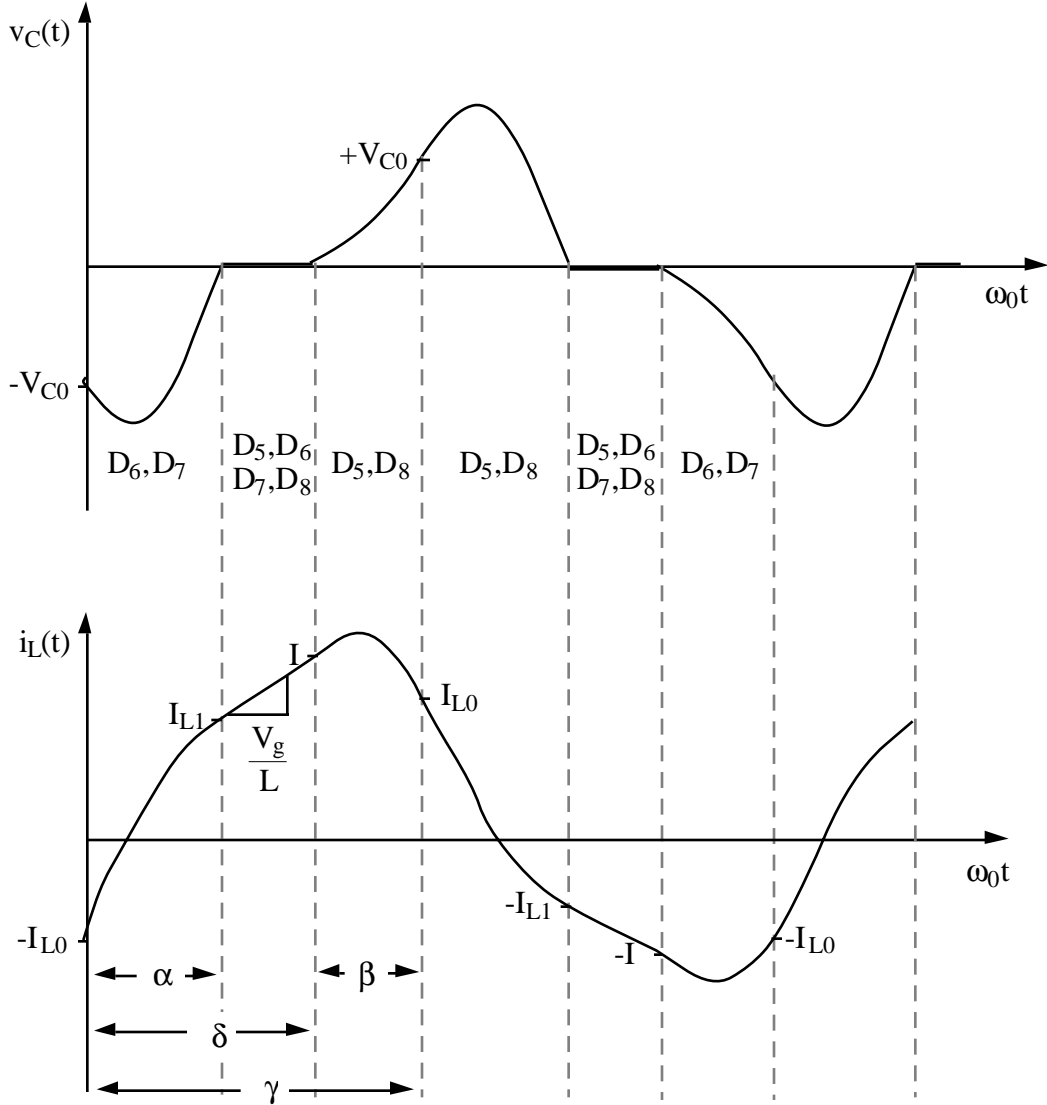


Fig. 5.21. Discontinuous conduction mode waveforms.

$$\begin{aligned}
 M_{C0} &= 1 - \cos(\beta) \\
 J_{L0} &= J + \sin(\beta) \\
 \cos(\alpha + \beta) - 2 \cos(\alpha) &= -1 \\
 -\sin(\alpha + \beta) + 2 \sin(\alpha) + (\delta - \alpha) &= 2J \\
 \beta + \delta &= \gamma \\
 M &= 1 + \left(\frac{2}{\gamma}\right)(J - \delta)
 \end{aligned}
 \tag{5-45}$$

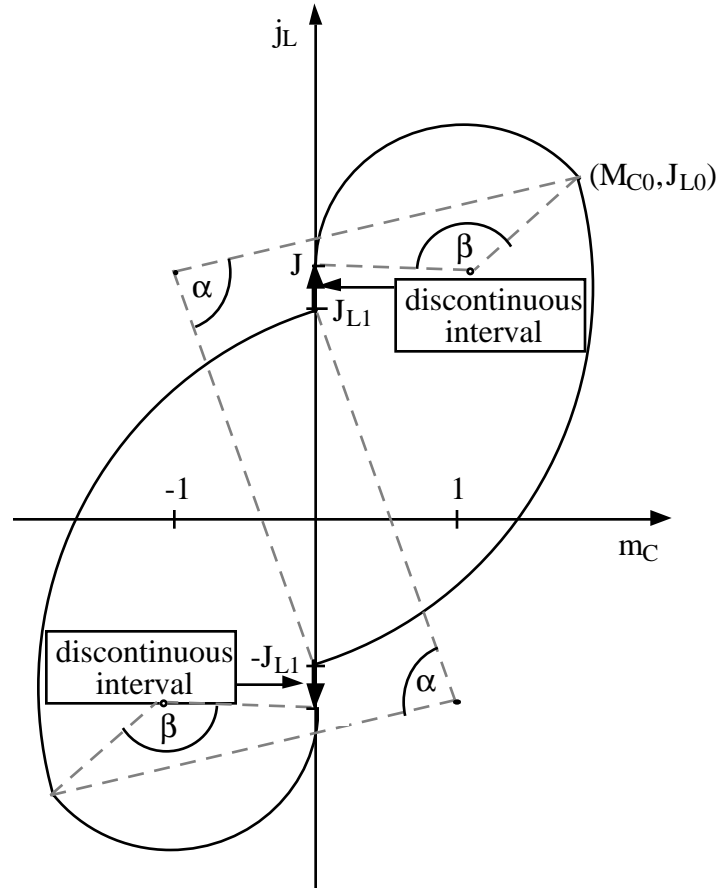


Fig. 5.22. State plane diagram, discontinuous conduction mode.

Unfortunately, the solution to this set of equations is not known in closed form, because of the mixture of linear and trigonometric terms. In consequence, the equations must be solved iteratively. For a given  $g$  and  $J$ , a computer is used to iteratively find the angles  $a$ ,  $b$ , and  $d$ .  $M$  is then evaluated, and the output plane characteristics can be plotted. The result is given in Fig. 5.23. The dotted lines are the DCM solutions, and the solid lines are the valid CCM solutions. Figure 5.23 describes the complete dc behavior of the parallel resonant converter for all switching frequencies above  $f_0/2$ .

Note that the DCM solutions curve up sharply near the  $J$ -axis. The short-circuit current can be shown to be

$$J_{SC} = J|_{M=0} = \frac{\gamma}{2} \quad (5-46)$$

This current is somewhat greater than the value (incorrectly) predicted by the continuous conduction mode solution.

It should be noted that there is another type of discontinuous conduction mode which can occur in the parallel resonant converter. This mode occurs due to the switching ripple in the output filter inductor current, and is similar to the discontinuous conduction mode in PWM converters. It

occurs at light load (low  $J$ ), when the dc component of output current is less than the peak magnitude of the filter inductor current ripple. This condition leads to an additional subinterval during which all four output rectifier diodes are reverse-biased. Its effect on the output characteristics is to cause the output voltage to increase at light load.

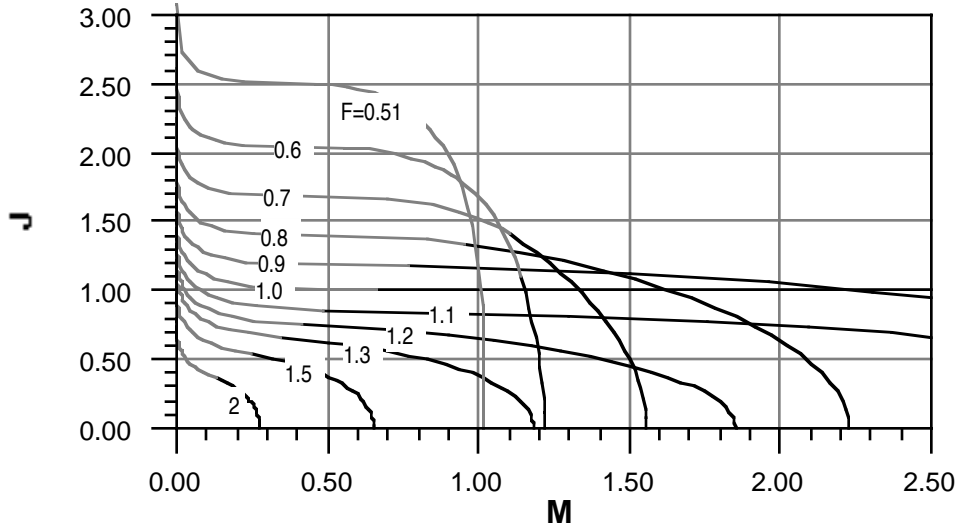


Fig. 5.23. Complete output characteristics of the parallel resonant converter, valid in both CCM and DCM, for  $F > 0.5$ . Solid curves: CCM. Dotted curves: DCM.

### 5.3. Design Considerations

In this section, the analyses and results of the previous two sections are extended to include component stresses. Some simple arguments are given, which explain how the peak component stresses of the parallel resonant converter in the CCM depend on load voltage but not load current. These results are applied to design a simple off-line dc-dc converter; detailed sample calculations are given.

#### Peak component stresses

It can be shown that the normalized peak tank capacitor voltage is

$$M_{Cp} = \begin{cases} \sqrt{(M_{C0} + 1)^2 + (J - J_{L0})^2} - 1 & \text{when } (J_{L0} > J) \\ \sqrt{1 + (J_{L1} - J)^2} + 1 & \text{when } (J_{L0} < J) \end{cases} \quad (5-47)$$

for the continuous conduction mode, and is given by the following expression for the discontinuous conduction mode:

$$M_{Cp} = \begin{cases} \sqrt{(M_{C0} + 1)^2 + (J - J_{L0})^2} - 1 & \text{when } (J_{L0} > J) \\ 2 & \text{when } (J_{L0} \leq J) \end{cases} \quad (5-48)$$

It also can be shown that the normalized peak tank inductor current, which coincides with the peak transistor current, is

$$J_{Lp} = \begin{cases} J_{L0} & \text{when } (M_{C0} < 1 \text{ and } J_{L0} > 0) \\ J + \sqrt{(J_{L1} - J)^2 + 1} & \text{when } (M_{C0} > 1 \text{ or } J_{L0} < 0) \end{cases} \quad (5-49)$$

This expression is valid only for CCM. For DCM, the corresponding expression is

$$J_{Lp} = \begin{cases} J_{L0} & \text{when } (\gamma - \delta < \pi/2) \\ J + 1 & \text{when } (\gamma - \delta \geq \pi/2) \end{cases} \quad (5-50)$$

The derivation of these results, by state plane analysis, is omitted here. The normalized peak tank inductor current is plotted in Fig. 5.25(a) and 5.25(b), for both CCM and DCM, and the normalized peak tank capacitor voltage is plotted in Fig. 5.26. It can be seen that, in the CCM, the peak tank inductor current characteristics are nearly vertical lines; i.e., the peak currents are approximately proportional to the output voltage, and are nearly independent of output current. In the DCM, the situation is reversed, and peak current is approximately proportional to load current instead of load voltage.

This behavior is quite unusual, because it implies that in CCM, decreases in load current do not cause corresponding decreases in transistor currents or in conduction losses. Its origin can be understood using the approximate sinusoidal arguments of chapter 2. By use of the volt-second balance principle on the output filter inductor, we know that the dc output voltage is equal to the average rectified tank capacitor voltage:

$$V = \langle |v_C| \rangle \quad (5-51)$$

If the  $v_C(t)$  waveform is sinusoidal, then the relation between its peak value and its average rectified value is

$$M_{Cp} \cong \frac{\pi}{2} M \quad (5-52)$$

Equation (5-52) is a quite good approximation, except in the discontinuous conduction mode or near the mode boundary. It states that the peak capacitor voltage is directly related to the load voltage, and there is very little dependence on the load current. Indeed, the peak-to-average ratio of the exact tank capacitor ac voltage waveform exhibits only a second-order dependence on the load current in the continuous conduction mode.

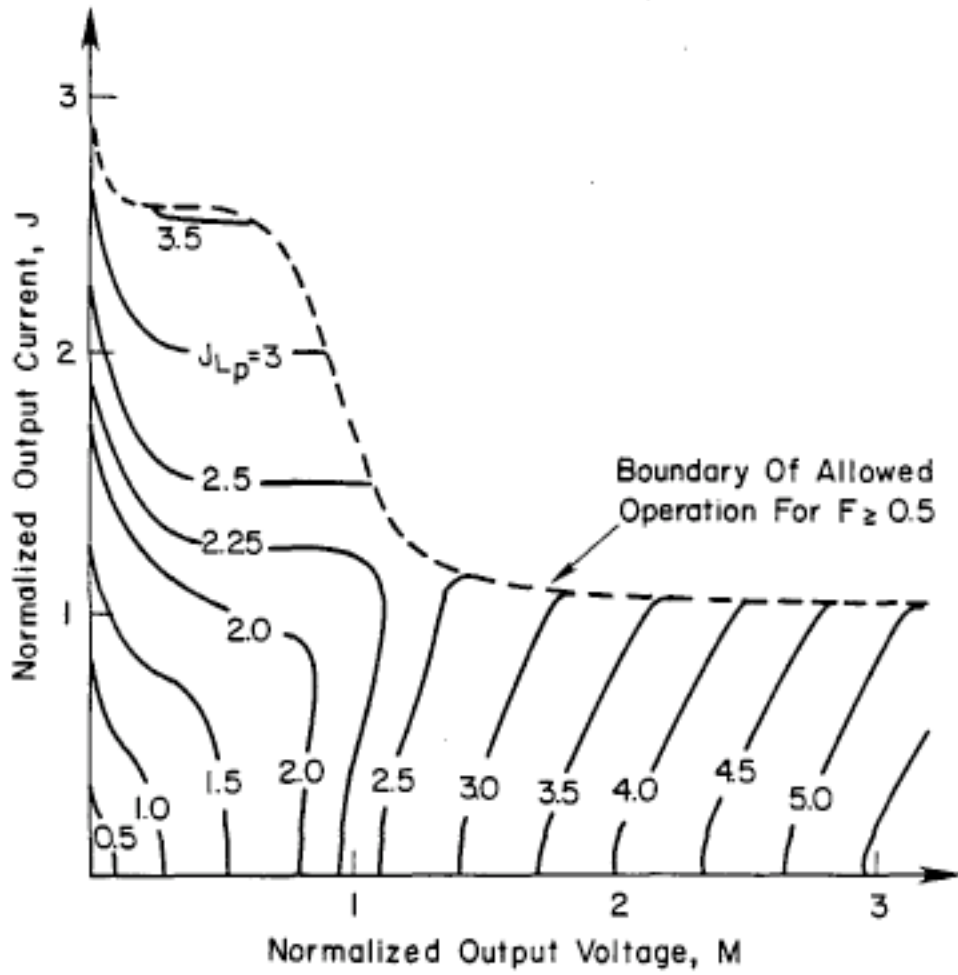


Fig. 5.25(a) Curves of constant  $J_{Lp}$ , valid for both CCM and DCM, in the single frequency region of the output plane and above the peak frequency in the double frequency region.

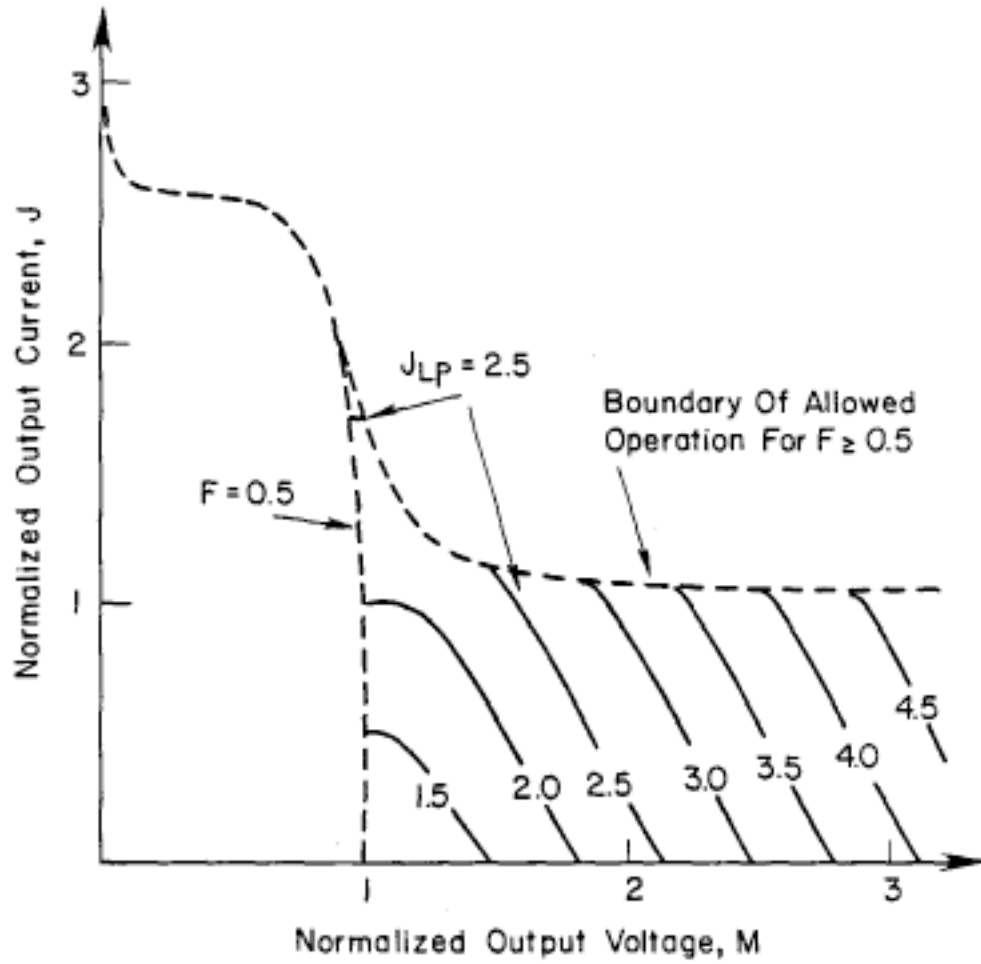


Fig. 5.25(b) Curves of constant  $J_{LP}$ , valid for both CCM and DCM, below the peak frequency in the double frequency region of the output plane.

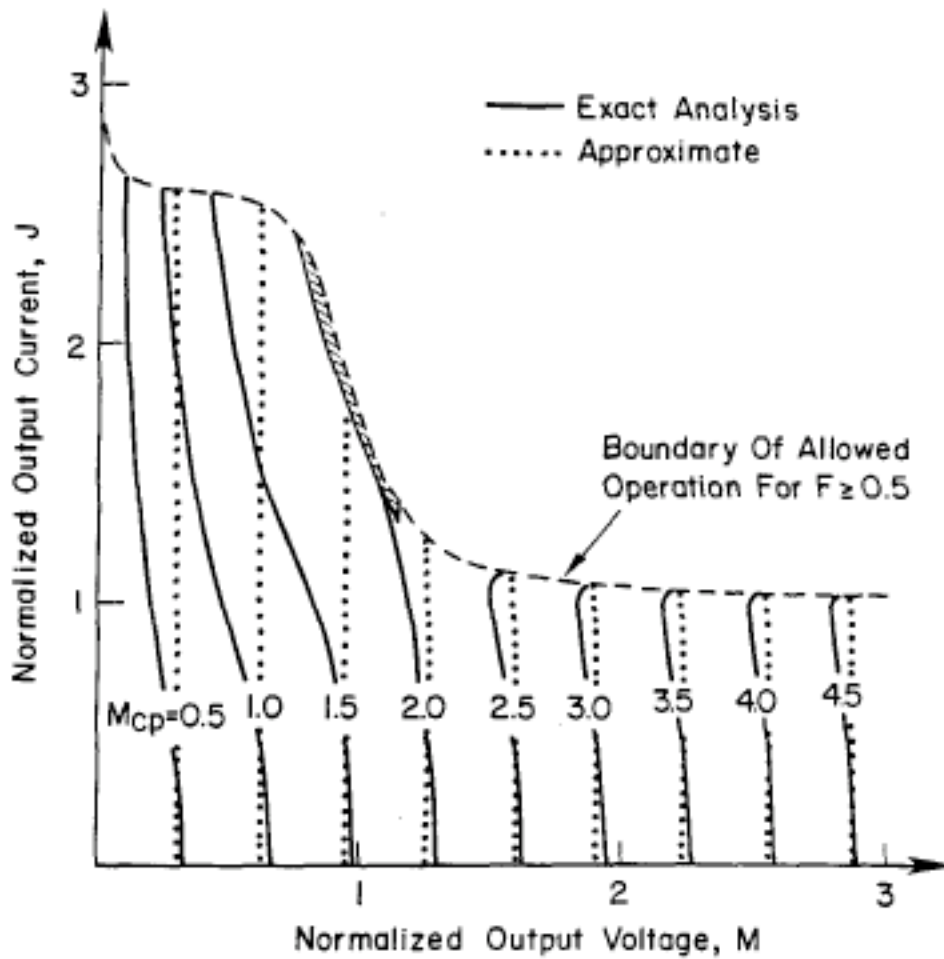


Fig. 5.26(a) Curves of constant  $M_{Cp}$ , valid for both CCM and DCM, in the single frequency region of the output plane and above the peak frequency in the double frequency region.

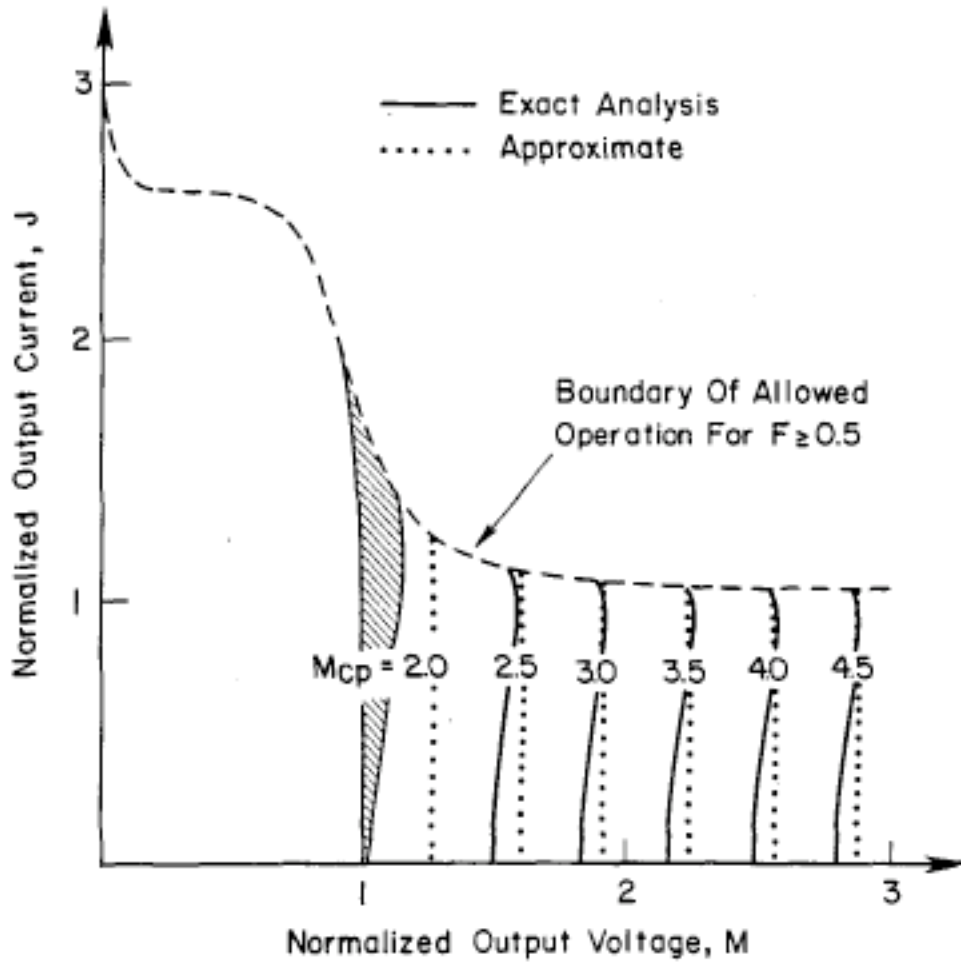


Fig. 5.26(b) Curves of constant  $M_{Cp}$ , valid for both CCM and DCM, below the peak frequency in the double frequency region of the output plane.

So to maintain the output voltage, the tank capacitor must be charged each cycle to a peak value of  $V_{Cp} \cong V\pi/2$ . This charge must be supplied by the tank inductor, and hence the peak tank inductor current (with transformer turns ratio of 1:1) is approximately

$$I_{Lp} \cong \frac{\pi}{2} \frac{V}{R_0} \quad (5-53)$$

or in normalized form,

$$J_{Lp} \cong \frac{\pi}{2} M \quad (5-54)$$

Again, these approximations are reasonably accurate only for the continuous conduction mode. Hence, the peak inductor and transistor currents are also proportional to the output voltage, and exhibit only a second-order dependence on the load current.

For the usual dc voltage regulator application, it is unfortunate that Eq. (5-53) is true. In this application, the output voltage  $V$  is regulated to be constant and independent of load current.

The peak transistor current therefore is essentially independent of the load current. The characteristic impedance  $R_0$  must be chosen such that the desired full-load output current is obtained; if the worst-case operating point (maximum load current  $I_{\max}$  and minimum input voltage  $V_{g\min}$ ) is chosen to correspond to the output plane point ( $M_{\max}, J_{\max}$ ), then  $R_0$  must be chosen as

$$R_0 = J_{\max} \frac{V_{g\min}}{I_{\max}} \quad (5-55)$$

According to Fig. 5.24, operation of the converter with large values of  $J$  is not possible, and typical values of  $J_{\max}$  are close to unity. In consequence, according to Eq. (5-55), for a specified  $V_{g\min}$  and  $I_{\max}$  the maximum allowable value of  $R_0$  is limited.

The peak transistor current (with a 1:1 transformer turns ratio) at this operating point can now be estimated by plugging Eq. (5-55) into Eq. (5-53), to obtain

$$I_{Lp} \cong \frac{\pi}{2} \frac{V I_{\max}}{V_{g\min} J_{\max}} \quad (5-56)$$

This predicts that the peak transistor current does not vary with  $I$  or  $V_g$ , but depends only on the worst-case values  $I_{\max}$  and  $V_{g\min}$ . To the extent that Eq. (5-53) is a good approximation, the peak current is essentially unchanged as the load current is reduced. In fact, depending on the design, the exact peak current given by Eq. (5-49) may even increase somewhat as the load current is reduced. Furthermore, it can be seen from Eq. (5-56) that, to minimize  $I_{Lp}$ ,  $J_{\max}$  should be chosen as large as possible.

### ***Design example: Off-line dc-dc converter***

Let us next consider the design of a transformer-isolated dc-dc parallel resonant converter, to meet the following specifications:

$$\begin{aligned} \text{input voltage:} & \quad V_g = 270\text{Vdc} \pm 20\% \\ \text{so} & \quad V_{g\max} \geq V_g \geq V_{g\min} \\ \text{with} & \quad V_{g\max} = 324\text{V} \\ & \quad V_{g\min} = 216\text{V} \end{aligned}$$

$$\begin{aligned} \text{output voltage:} & \quad \text{regulated } 5\text{Vdc} \\ \text{so} & \quad V = 5\text{V} \end{aligned}$$

$$\begin{aligned} \text{load current:} & \quad \text{max. load current } I_{\max} = 40\text{A} \\ & \quad \text{min. load current } I_{\min} = 4\text{A} \\ \text{so} & \quad I_{\max} \geq I \geq I_{\min} \end{aligned}$$

$$\text{maximum switching frequency:} \quad f_{s\max} = 1 \text{ MHz}$$

Operate MOSFET devices with zero voltage switching.

As in the case of the series resonant converter, these specifications imply that the locus of possible operating points is the trapezoid of Fig. 5.27. The voltage conversion ratio  $M$  can vary over the range

$$M_{\max} \geq M \geq M_{\min} \quad (5-57)$$

where

$$M_{\max} = \frac{V}{n V_{g\min}}$$

$$M_{\min} = \frac{V}{n V_{g\max}}$$

and the transformer turns ratio is 1:n

For a given value of  $M$ , the normalized load current  $J$  can vary over the range

$$M n^2 R_0 \frac{I_{\min}}{V} \leq J \leq M n^2 R_0 \frac{I_{\max}}{V} \quad (5-58)$$

or,

$$\frac{M}{Q_{\max}} \leq J \leq \frac{M}{Q_{\min}}$$

with

$$Q = \frac{R}{n^2 R_0}$$

Equations (5-57) and (5-58) describe the trapezoid of Fig. 5.27. The maximum value of  $J$  is therefore

$$J_{\max} = M_{\max} n^2 R_0 I_{\max} / V = n R_0 I_{\max} / V_{g\min} \quad (5-59)$$

The converter design problem involves choice of  $L$ ,  $C$ , and  $n$ , such that the specifications are met and a good design is obtained. This is equivalent to selecting  $n$ ,  $R_0$ , and  $f_0$ , or alternatively  $M_{\max}$ ,  $J_{\max}$ , and  $f_0$ , since these quantities are all related by the following equations and definitions:

$$L = \frac{R_0}{2\pi f_0} \quad (5-60)$$

$$C = \frac{1}{2\pi f_0 R_0}$$

$$f_0 = \frac{f_{s\max}}{F_{\max}}$$

$$n = \frac{V}{M_{\max} V_{g\min}}$$

$$R_0 = \frac{J_{\max} V_{g\min}}{n I_{\max}} = J_{\max} M_{\max} \frac{V_{g\min}^2}{V I_{\max}}$$

Hence, the designer is free to choose  $M_{\max}$  and  $J_{\max}$  to be any point in the output plane for which the converter has a solution. The converter steady-state output characteristics can then be used to find  $F$  at this point, and Eqs. (5-60) can be used to determine  $L$ ,  $C$ , and  $n$ . Thus the design problem is reduced to selection of  $M_{\max}$  and  $J_{\max}$ .

As with all design problems, there is no single correct answer, and the engineer must evaluate several tradeoffs. It is generally desired to select  $M_{\max}$  and  $J_{\max}$  such that (1) the peak component stresses are low, (2) the range of switching frequency variations is moderate, (3) the converter is able to operate with the specified range of variations in  $I$  and  $V_g$ , (4) zero voltage switching is obtained throughout the specified range, and (5) the converter is tolerant of expected parasitic element values. One good approach to arrive at a suitable tradeoff is to use a computer spreadsheet for evaluation of component values and stresses as a function of the choice of  $M_{\max}$  and  $J_{\max}$ . Several values can be tried, and the best tradeoff can usually be quickly found. A sample set of calculations which illustrates how to set up such a spreadsheet is given here.

Zero current switching occurs for operation below resonance with  $J \leq 1$ . Zero voltage switching occurs when the converter operates above resonance, or below resonance with  $J > 1$ . Since for this example it is specified that the converter should operate with zero voltage switching, let us choose to operate the converter above resonance, i.e., with  $F \geq 1$ .

As noted previously, the above-resonance CCM characteristics are restricted to  $J \leq 1$ . It was also previously noted that peak current stresses are minimized by maximizing  $J$ . Hence,  $J_{\max}$  should be chosen close to unity. To allow a small margin to account for tolerances in the tank element values, let us choose  $J_{\max} = 0.9$ .

The choice of  $M_{\max}$  is more dependent on the specific application requirements. Increasing  $M_{\max}$  causes the converter switching frequency to be closer to resonance. In consequence, the converter effective  $Q$ -factor is increased, the tank characteristic impedance is decreased, and the range of switching frequency variations required to regulate the load voltage is reduced. The resulting design will exhibit a smaller tank inductance, a larger tank capacitance, and a lower transformer turns ratio. These points are discussed in more detail later in this section.

Let us make the somewhat arbitrary choice  $M_{\max} = 1.2$ . The converter operating region is then as shown in Fig. 5.28. The values of normalized switching frequency  $F$  at the various operating points can now be estimated graphically from this figure, or they can be solved exactly by numerical iteration of Eqs. (5-31) and (5-35) to solve for  $g = \pi/F$  at the various given values of  $M$  and  $J$ . The results are listed in Table 5.2.

**Table 5.2.Design example: summary of converter behavior at various operating points**

point	V <sub>g</sub>	I	M	J	F	f <sub>s</sub> , kHz	I <sub>Lpk</sub>	V <sub>Cpk</sub>	
A	216	40	1.2	0.90	1.06	746	2.02	437	ZVS
B	216	4	1.2	0.09	1.29	911	2.28	400	ZVS
C	324	4	0.8	0.06	1.42	1000	2.56	398	ZVS
D	324	40	0.8	0.60	1.26	884	2.49	426	ZVS

It can be seen from Fig. 5.28 and Table 5.2 that the maximum value of F occurs at point C, for which F = 1.42. Since the maximum switching frequency is specified to be 1 MHz, we should therefore choose the tank resonant frequency f<sub>0</sub> to be

$$f_0 = \frac{f_{s\max}}{F_{\max}} = \frac{1 \text{ MHz}}{1.42} = 704 \text{ kHz} \quad (5-61)$$

The minimum switching frequency occurs at point A, where F<sub>A</sub> = 1.06. The value is

$$f_{s\min} = f_0 F_A = (704 \text{ kHz})(1.06) = 746 \text{ kHz} \quad (5-62)$$

The transformer and filter components must be sized to operate at this minimum frequency.

The characteristic impedance R<sub>0</sub> is found by evaluation of Eq. (5-55):

$$R_0 = J_{\max} \frac{V_{g\min}}{I_{\max}} = (0.9) \frac{(216\text{V})}{(40\text{A})} = 252\Omega \quad (5-63)$$

The values of L, C, and n can also now be evaluated using Eq. (5-60):

$$L = \frac{R_0}{2\pi f_0} = \frac{(252\Omega)}{2\pi (704 \text{ kHz})} = 57 \mu\text{H} \quad (5-64)$$

$$C = \frac{1}{2\pi f_0 R_0} = \frac{1}{2\pi (704 \text{ kHz}) (252\Omega)} = 900 \text{ pF}$$

$$n = \frac{V}{M_{\max} V_{g\min}} = \frac{(5\text{V})}{(1.2)(216\text{V})} = 0.0193$$

An NPO-type multilayer ceramic capacitor would typically be used in this application.

The peak tank inductor current and peak tank capacitor voltage, both referred to the transformer primary, are computed next. These quantities can be calculated at each operating point by evaluation of Eqs. (5-47) and (5-49), and by use of Eqs. (5-31) through (5-34) to find the intermediate variables j, J<sub>L1</sub>, J<sub>L0</sub>, and M<sub>C0</sub>. For example, at point A, we have

$$\gamma = \frac{\pi}{F} = \frac{\pi}{(1.06)} = 2.96 \text{ radians} \quad (5-65)$$

$$\begin{aligned}\varphi &= -\cos^{-1}\left(\cos\left(\frac{\gamma}{2}\right) + J \sin\left(\frac{\gamma}{2}\right)\right) \\ &= -\cos^{-1}\left(\cos\left(\frac{2.96 \text{ rad}}{2}\right) + (0.9) \sin\left(\frac{2.96 \text{ rad}}{2}\right)\right) \\ &= -0.17 \text{ radians}\end{aligned}$$

$$J_{L1} = -\frac{\sin \varphi}{\cos\left(\frac{\gamma}{2}\right)} = -\frac{\sin(-0.17 \text{ rad})}{\cos\left(\frac{2.96 \text{ rad}}{2}\right)} = 1.95$$

$$J_{L0} = -(J^2 - 1) \tan\left(\frac{\gamma}{2}\right) = -((0.9)^2 - 1) \tan\left(\frac{2.96}{2}\right) = 2.14$$

$$M_{C0} = \frac{-J \sin \varphi}{\cos\left(\frac{\gamma}{2}\right)} = \frac{-(0.9) \sin(-0.17 \text{ rad})}{\cos\left(\frac{2.96 \text{ rad}}{2}\right)} = 1.76$$

$$\begin{aligned}J_{Lp} &= J + \sqrt{(J_{L1} - J)^2 + 1} \quad \text{since } M_{C0} > 1 \\ &= (0.9) + \sqrt{((1.95) - (0.9))^2 + 1} \\ &= 2.35\end{aligned}$$

$$I_{Lp} = J_{Lp} I_{\text{base}} = J_{Lp} \frac{V_g}{R_0} = (2.35) \frac{(216\text{V})}{(252\Omega)} = 2.02\text{A}$$

$$\begin{aligned}M_{Cp} &= \sqrt{(M_{C0} + 1)^2 + (J - J_{L0})^2} - 1 \quad \text{since } J_{L0} > J \\ &= \sqrt{((1.76) + 1)^2 + ((0.9) - (2.14))^2} - 1 \\ &= 2.02\end{aligned}$$

$$V_{Cp} = M_{Cp} V_{\text{base}} = M_{Cp} V_g = (2.02) (216\text{V}) = 436.89\text{V}$$

Similar computations can be performed to find the peak stresses at other operating points. The results are summarized in Table 5.2. It can be seen that the peak current occurs at point C, and is equal to 2.56A, while the peak tank capacitor voltage occurs at point A, and is equal to about 437V. The minimum switching frequency is 746kHz.

For comparison, designs using the same specifications but different choices of  $M_{\text{max}}$  and/or  $J_{\text{max}}$  are summarized in Table 5.3. The first line is a summary of the design given above, with  $M_{\text{max}} = 1.2$  and  $J_{\text{max}} = 0.9$ . In the second line, the effect of increasing  $M_{\text{max}}$  to 2.5 is given. It can be seen that this results in reduced switching frequency variation, as well as a small reduction in peak current. However, this performance comes at the expense of a substantial increase in peak tank capacitor voltage. In a similar manner, as seen on the third line of the table, decreasing  $M_{\text{max}}$  to 0.5 causes the switching frequency variation and peak current to be increased, but allows

reduction of the peak tank capacitor voltage. The fourth and fifth lines reveal the effect of decreasing  $J_{\max}$ . It can be seen that this causes the peak current to be increased, with very little influence on the peak tank capacitor voltage. The minimum switching frequency is increased slightly.

**Table 5.3. Converter performance vs.  $M_{\max}$  and  $J_{\max}$**

$M_{\max}$	$J_{\max}$	min. $f_s$	L	C	1/n	pri $I_{pk}$	pri $V_{Cpk}$
1.2	0.9	746 kHz	57 $\mu$ H	900 pF	52	2.56 A	437 V
2.5	0.9	856 kHz	102 $\mu$ H	370 pF	107	2.12 A	871 V
0.5	0.9	577 kHz	31 $\mu$ H	2.8 nF	22	4.31 A	213 V
1.2	0.75	800 kHz	48 $\mu$ H	1.1 nF	52	3.07 A	427 V
1.2	0.5	846 kHz	32 $\mu$ H	1.6 nF	52	4.60 A	412 V

#### 5.4. A high voltage parallel resonant converter

The parallel resonant converter is particularly well suited to applications involving high voltage dc outputs. In this application, the winding capacitance and leakage inductance of the step-up transformer, as well as secondary-side capacitances, typically have a profound effect on the converter behavior. In switched-mode converters, the leakage inductance causes undesirable voltage spikes during the transistor turn-off transition, which can damage circuit components. Also, the winding capacitance leads to current spikes at the transistor turn-on transition and slow voltage rise times. Both nonidealities typically lead to greatly increased switching and/or snubber losses, with reduced converter efficiency and reliability. The parallel resonant converter avoids these problems, because the transformer leakage inductance and winding capacitance can be incorporated directly into the basic converter operation, and can wholly or partially replace the resonant tank elements. The converter waveforms then closely follow their ideal textbook shapes, and the converter operates efficiently and reliably. Indeed, other topologies such as PWM or even the series resonant converter, when used in a high voltage application with a non ideal transformer, are likely to exhibit parallel resonant converter behavior, whether intended or not. This is true because the transformer nonidealities form a parallel tank circuit.

The design and operation of a high voltage parallel resonant converter is outlined here, for the following specifications:

<i>input voltage</i>	24 volts
<i>output voltage</i>	8 kV
<i>output current</i>	1 mA

### ***Simple high voltage transformer model and its implications for the PRC***

The experimentally measured impedance of a high voltage transformer, designed for use in a 24V input, 8kV at 1mA output dc-dc converter, is shown in Fig. 5.29. The measurement was made at the primary winding, with the secondary open-circuited. The transformer has a turns ratio of 1:68.75. The Bode plot shows the transformer primary self-inductance at frequencies below 15kHz. Evaluation of the low frequency asymptote yields the value 1.86mH, essentially equal to the magnetizing inductance referred to the primary side. Between 15kHz and 200kHz, the impedance appears capacitive. By evaluation of the asymptote, this effective winding capacitance is approximately 12pF referred to the secondary, or 0.055 $\mu$ F referred to the primary. This is a quite substantial amount of capacitance, and can severely degrade the operation of a PWM converter. The effects of the leakage inductance can be seen above 200kHz, where the impedance is again inductive. The asymptote predicts a total leakage inductance of 11 $\mu$ H referred to the primary. Additional resonances occur at yet higher frequencies.

This suggests that the transformer can be modelled by the lumped element circuit of Fig. 5.30. This model is valid for the given transformer at frequencies up to 400kHz, but breaks down at higher frequencies because the leakage inductance and winding capacitance are actually distributed parameters. However, this model does predict the behavior of a high voltage parallel resonant converter quite accurately.

Insertion of the transformer model into a half-bridge parallel resonant converter yields the circuit of Fig. 5.31. It can be seen that the leakage inductance is effectively in series with the tank inductance, and the winding capacitance is effectively in parallel with the tank capacitance. Provided that the parallel resonant converter can be designed to operate well with tank component values equal to or greater than the transformer model values, then transformer nonidealities do not degrade the operation of the circuit.

A voltage multiplier can easily be incorporated into the circuit, as shown in Fig. 5.31. The multiplier is current-driven, and allows reduction of the transformer turns ratio and diode voltage ratings, at the expense of increased output filter capacitance.

The output filter inductor  $L_f$  of the parallel resonant converter can become a large and expensive element in high voltage applications, comparable in size to the high voltage transformer. Fortunately, it is possible to remove this component altogether, without degrading the performance of the converter. Although this leads to a qualitative change in converter operation, it is still possible to obtain a good design, without increasing component size or peak currents. This is an important option for high voltage applications, and is incorporated into the converter of Fig. 5.31.

**The parallel resonant converter with no output filter inductor**

With the output filter inductor removed, the tank waveforms are modified as illustrated in Fig. 5.32. Several modes of operation can occur, depending on the order in which the semiconductor devices switch. A new analysis must be performed to solve this case, although the results do not differ greatly from those of sections 5.1 and 5.2. Such an analysis is given in [1] and is not repeated here. The result for one of the most important modes, mode 1, is

$$J = \frac{1}{2\gamma} \left[ \frac{1}{2}(1-M^2) (\gamma-\alpha)^2 + 2 (\gamma-\alpha) (1+M) \sqrt{M} - 2M \right] \quad (5-66)$$

with

$$\alpha = \cos^{-1} \left( \frac{1-M}{1+M} \right)$$

This mode occurs provided that

$$\sin(\alpha) + (\gamma - \alpha) \cos(\alpha) > 0 \quad (5-67)$$

and

$$\gamma > \alpha + \sin(\alpha)$$

Otherwise, the converter may operate in mode 2, mode 3, or another mode. The output characteristics for modes 1, 2, and 3 are plotted in Fig. 5.33. The converter operates in mode 1 under short-circuit conditions, and hence the short-circuit output current can be found by substitution of  $M=0$  into Eq. (5-66). The result is  $J_{SC} = g/4 = \pi/4F$ . The converter is again capable of both increase and decrease of the output voltage with respect to the input voltage, and large output voltages with near current-source characteristics are obtained near resonance. Analysis of modes 1, 2, and 3, including output characteristics, mode boundaries, conduction losses, and peak component stresses, is given in [1].

**5.5. A Low Harmonic Rectifier**

Another application of the parallel resonant converter is as a low harmonic rectifier, in which the converter input voltage  $v_g(t)$  is a rectified ac line voltage of the form  $V_{gpk} |\sin \omega t|$ , and the converter input current is controlled, by variation of the switching frequency, to follow the input voltage. The input current  $i_g(t)$  is then of the form  $v_g(t) / R_e$ , where  $R_e$  is the “emulated resistance” of the input port. The output is an essentially constant dc voltage  $V$ .

The use of the parallel resonant converter in this application has several advantages. The use of zero-current- or zero-voltage-switching allows the use of IGBT's at switching frequencies of 20-200kHz with high efficiency. A 1.4kW transformer-isolated PRC rectifier has been reported using IGBT's switching at 45-75kHz, with a full-load efficiency of 93.8% [8]. When operated above resonance, the converter can operate with both buck and boost voltage conversion ratios, and hence inrush current limiting is possible. Transformer isolation is easily obtained, and the converter can operate ideally with significant transformer leakage inductance. The output rectifier diodes switch at zero voltage, and also do not lead to switching loss. The converter naturally exhibits a high impedance input, and hence the open-loop input current waveforms are closer to sinusoidal [7] than are the peak-detection-type waveforms of the open-loop PWM boost converter. Hence, the converter is easier to control, and a high quality input current waveform can be obtained with a simple and lower-bandwidth control loop. The converter output current is nonpulsating.

With these advantages come some disadvantages. Many of the converter losses are independent of the load current, and hence the converter efficiency at light load is relatively low. The converter peak currents are higher than in PWM approaches. The converter requires a high-quality tank capacitor, usually a multilayer ceramic of the NPO type. The input current is pulsating, and hence an input EMI filter is required. For a given application, these disadvantages must be weighed against the advantages listed above.

In this section, the behavior of the parallel resonant converter in low harmonic rectifier applications is discussed.

### ***Rectifier analysis***

In design of a low harmonic rectifier, the converter input characteristic (input current  $i_g$  vs. input voltage  $v_g$ ) is of major interest. It is desired that this characteristic be linear and resistive in nature. From this characteristic, one can deduce how the closed-loop switching frequency and other quantities must vary as the ac input voltage changes, so that such a linear resistive characteristic is attained. The analysis of the preceding part of this chapter, in which the output characteristics are determined, is not well-suited for rectifier design. Since the waveforms are normalized using the input voltage  $v_g(t)$  as the base voltage, all normalized quantities diverge at the zero crossings of the input voltage waveform. Furthermore, since the base voltage  $v_g(t)$  varies with time, the actual waveforms do not have the same shape as the normalized quantities. Hence, the results of the preceding dc-dc converter analysis need to be adapted to be better suited for the ac-dc rectifier case.

To avoid the problem of divergence at the input voltage zero crossings, it is necessary to choose a different (constant) quantity as the base voltage for normalization. A suitable quantity is the dc output voltage  $V$ . All other base quantities can then be defined as in Table 5.4. A

transformer with 1:n turns ratio is assumed, and base quantities are given with respect to both the transformer primary and secondary. The rectifier terminal waveforms are then as given in Table 5.5.

**Table 5.4. Normalizing base quantities, rectifier applications**

	primary	secondary
base impedance	$R_0 = \sqrt{L/C}$	$n^2 R_0$
base voltage	$V / n$	$V$
base current	$V / (n R_0)$	$V / (n^2 R_0)$
base power	$V^2 / (n^2 R_0)$	$V^2 / (n^2 R_0)$

**Table 5.5. Definition of rectifier normalized terminal signals**

	normalized quantity	basic quantity
ac input voltage	$m_g(t) = n v_g(t) / V$	$v_g(t) = m_g(t) V / n$
ac input current	$j_g(t) = i_g(t) n R_0 / V$	$i_g(t) = j_g(t) V / n R_0$
dc output voltage	1	$V$
dc output current	$j(t) = n^2 R_0 i(t) / V$	$i(t) = j(t) V / n^2 R_0$

The definitions of Tables 5.4 and 5.5 can be substituted into the converter solution, Eqs. (5-31) and (5-35), to obtain the following expression for the rectifier normalized input characteristic in the continuous conduction mode:

$$\varphi = \begin{cases} -\cos \left[ j_g \sin \left( \frac{\gamma}{2} \right) + \cos \left( \frac{\gamma}{2} \right) \right] & \text{for } 0 < \gamma < \pi \\ +\cos \left[ j_g \sin \left( \frac{\gamma}{2} \right) + \cos \left( \frac{\gamma}{2} \right) \right] & \text{for } \pi < \gamma < 2\pi \end{cases} \quad (5-68)$$

$$m_g = \frac{\gamma}{2} \frac{1}{\sin \varphi - \frac{\cos(\gamma/2)}{\cos(\gamma/2)}} \quad (5-69)$$

The rectifier operates in continuous conduction mode provided that

$$j_g < j_{g\text{crit}} \quad (5-70)$$

where  $j_{g\text{crit}} = -\frac{1}{2} \sin(\gamma) + \sqrt{\sin^2 \left( \frac{\gamma}{2} \right) + \frac{1}{4} \sin^2(\gamma)}$

Equation (5-45) can be adapted in a similar manner to find the discontinuous conduction mode rectifier characteristics.

The complete parallel resonant converter input characteristics are plotted in Fig. 5.34. These characteristics show how the input current will vary, as a function of the input voltage and switching frequency. For example, consider the open loop case with  $F = 0.8$ . If the applied input voltage is a rectified sinusoid, so that  $m_g(t) = nv_g(t)/V$  is of the form

$$m_g(t) = M_{gpk} |\sin(\omega t)| \tag{5-71}$$

then  $m_g$  varies between zero and  $M_{gpk}$ . The  $F = 0.8$  characteristic is used to find the resulting open-loop input current. The result for  $M_{gpk} = 0.9$  is shown in Fig. 5.35. when  $m_g$  is less than approximately 0.44, there is no converter solution and the input current remains at zero. The input current then rises quickly, and the input current assumes the flattened shape shown in the figure. While there are substantial harmonics in this waveform, their magnitudes are nonetheless much lower than the peak-detection-type waveforms generated by open-loop PWM converters. As a result, it is easier to correct the input current waveform of PRC-based rectifiers than PWM-based rectifiers.

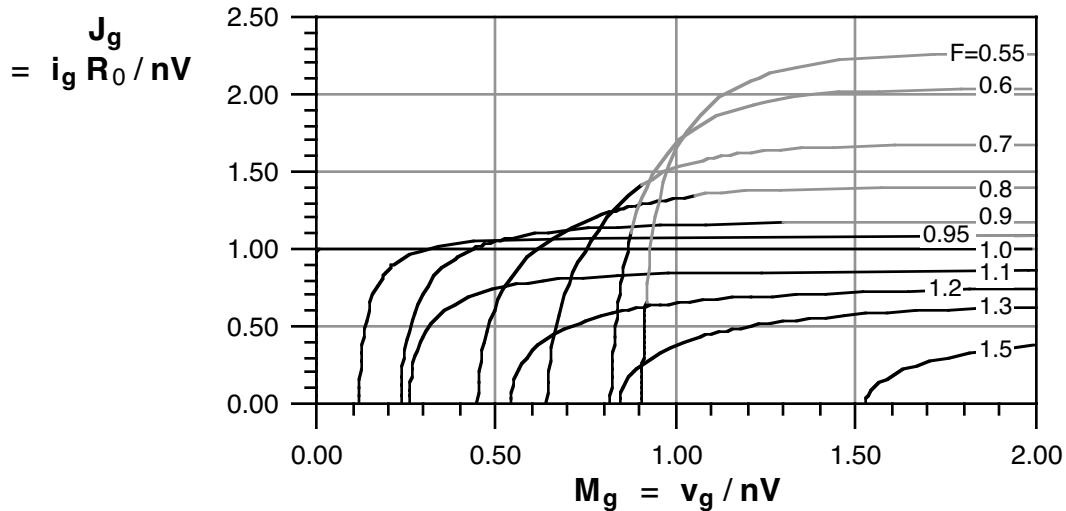


Fig. 5.34. Input characteristics of the parallel resonant converter. Solid lines: CCM solutions. Shaded lines: DCM solutions.

Fig. 5.35. Normalized input current waveform of the open-loop parallel resonant rectifier, for the case  $F = 0.8, M_{gpk} = 0.9$ .

The input line current harmonics are improved by use of a feedback loop which varies the switching frequency, to regulate the input current to be proportional to the input voltage. If this loop works perfectly, then the input current becomes

$$i_g(t) = \frac{v_g(t)}{R_e} \tag{5-72}$$

where  $R_e$  is the emulated resistance. In normalized form, Eq. (5-72) can be written

$$j_g(t) = m_g(t) \frac{R_0}{R_e} \quad (5-73)$$

This desired closed-loop linear resistive input characteristic is overlaid on the normalized converter input characteristics in Fig. 5.36. It can be seen from this plot how the switching frequency must be varied by the feedback loop.

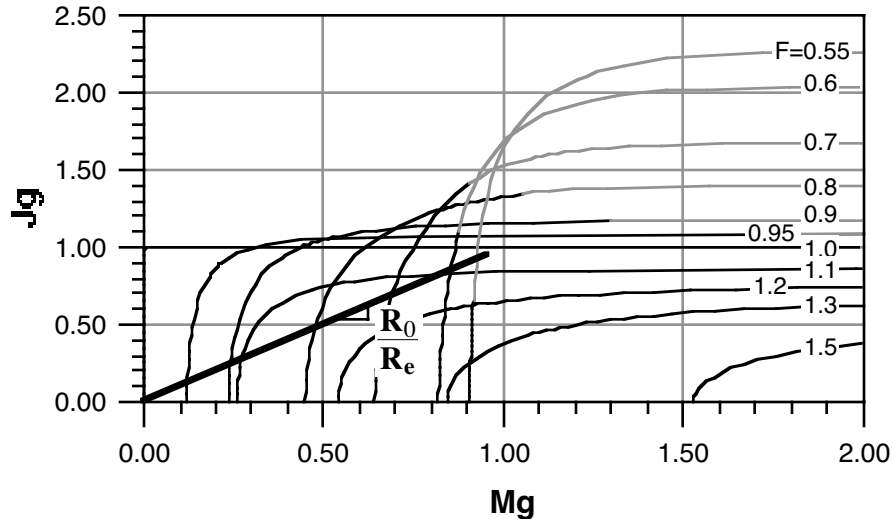


Fig. 5.36. Overlaying the desired resistive input characteristic on the converter input characteristics, to determine how the switching frequency will vary.

It can be seen that, if  $M_{gpk}$  and  $R_0/R_e$  are large enough, then the converter will operate in the discontinuous conduction mode near the peak of the input ac sinusoid. Also, there are no solutions when  $m_g$  is small and  $j_g$  is large. In consequence, for a given specified  $R_e$ , the designer must choose  $R_0$  sufficiently small, so that the converter operates in the valid range of converter solutions.

Zero current switching occurs for operation below resonance with  $j_g < 1$ . Otherwise, the converter operates with zero voltage switching. There are no solutions above resonance with  $j_g > 1$ .

### **Rectifier component stresses**

The peak tank inductor current and peak tank capacitor voltage can be found by adapting Eqs. (5-47) to (5-50).

$$M_{Cp} = \frac{V_{Cp}}{V} = \begin{cases} m_g \left( \sqrt{\left( j_g \frac{\sin \varphi}{\cos \frac{\gamma}{2}} - 1 \right)^2 + \left( j_g + (j_g^2 - 1) \tan \frac{\gamma}{2} \right)^2} - 1 \right) & \text{when } \left( - (j_g^2 - 1) \tan \frac{\gamma}{2} > J \right) \\ \sqrt{1 + (J_{L1} - J)^2} + 1 & \text{when } (J_{L0} < J) \end{cases}$$

## REFERENCES

- [1] Steven D. Johnson, "Steady-State Analysis and Design of the Parallel Resonant Converter," M.S. Thesis, University of Colorado, Boulder, 1986.
- [2] S. D. Johnson and R. W. Erickson, "Steady-State Analysis and Design of the Parallel Resonant Converter," *IEEE Power Electronics Specialists Conference*, 1986 Record, pp. 154-165, June 1986. Also in *IEEE Transactions on Power Electronics*, vol. 3, no. 4, pp. 93-104, Jan. 1988.
- [3] R. L. Steigerwald, "High Frequency Resonant Transistor DC-DC Converters," *IEEE Transactions on Industrial Electronics*, vol. IE-31, no. 2, pp. 181-191, May 1984.
- [4] R. Oruganti and F. C. Lee, "State-Plane Analysis of the Parallel Resonant Converter," *IEEE Power Electronics Specialists Conference*, 1985 Record, pp. 56-73, June 1985.
- [5] V. Vorperian and S. Cuk, "Small-Signal Analysis of Resonant Converters," *IEEE Power Electronics Specialists Conference*, 1983 Record, pp. 269-282, June 1983.
- [6] S. D. Johnson, A. F. Witulski, and R. W. Erickson, "A Comparison of Resonant Topologies in High Voltage Applications," *IEEE Applied Power Electronics Conference*, 1987 Proceedings, pp. 145-156, March 1987. Also in *IEEE Trans. on Aerospace and Electronic Systems*, vol. AES-24, no. 3, pp. 263-274, July 1988.
- [7] M. J. Schutten, R. L. Steigerwald, and M. H. Kheraluwala, "Characteristics of Load Resonant Converters Operated in a High Power Factor Mode," *IEEE Applied Power Electronics Conference*, 1991 Proceedings, pp. 5-16, March 1991.
- [8] J. Hong, E. Ismail, R. Erickson, and I. Khan, "Design of the Parallel Resonant Converter as a Low Harmonic Rectifier," *IEEE Applied Power Electronics Conference*, 1993 Proceedings, pp. 833-840, March 1993.

## PROBLEMS

1. Derive the equations of the discontinuous conduction mode, Eqs. (5-45).
2. A full-bridge parallel resonant converter is to be used in a transformer-isolated off-line application, with the following specifications:
 

Input voltage $V_g$ :	270 – 390 volts
Output voltage $V$ :	5 volts
Output power $P$ :	50 – 500 watts
Maximum switching frequency:	1 MHz

 MOSFET's are to be used, with zero voltage switching.

- (a) Using the somewhat arbitrary choice  $M_{\max} = 1$ ,  $J_{\max} = 0.9$ , design a converter to meet these specifications. Specify: (i) the tank component values, referred to the primary side of the transformer, (ii) the transformer turns ratio, and (iii) the minimum switching frequency.
- (b) For your design of part (a), determine the peak tank inductor current and peak tank capacitor voltage at the four operating points
- $V_g = 270\text{V}$ ,  $P = 500\text{W}$
  - $V_g = 270\text{V}$ ,  $P = 50\text{W}$
  - $V_g = 390\text{V}$ ,  $P = 500\text{W}$
  - $V_g = 390\text{V}$ ,  $P = 50\text{W}$
- (c) By changing the choice of  $M_{\max}$  and/or  $J_{\max}$ , can you improve this design? How?